

Highlights

Spin vectors in the Koronis family: IV. Completing the sample of its largest members after 35 years of study

Stephen M. Slivan, Matthew Hosen Jr., Max Kurzner, Alyssa Sokol, Sarah Maynard, Anna V. Payne, Arden Radford, Alessondra Springmann, Richard P. Binzel, Francis P. Wilkin, Emily A. Mailhot, Alan H. Midkiff, April Russell, Robert D. Stephens, Vincent Gardiner, Daniel E. Reichart, Joshua Haislip, Aaron LaCluyze, Raoul Behrend, René Roy

- Koronis family spin vector sample completed to largest 32 members (~ 16 km diameter)
- Removal of sample selection biases for interpreting and modeling spin evolution
- The absence of prograde spins having rotation periods longer than about 20 h is real
- Smaller prograde objects avoided or escaped the spin-orbit trapping of larger objects
- Epochs analysis combined with convex inversion is effective to determine spin vectors

Spin vectors in the Koronis family: IV. Completing the sample of its largest members after 35 years of study

Stephen M. Slivan^{a,b,*}, Matthew Hosek Jr.^{c,1}, Max Kurzner^{d,2}, Alyssa Sokol^{d,3}, Sarah Maynard^b, Anna V. Payne^{b,4}, Arden Radford^{b,5}, Alessondra Springmann^{b,6}, Richard P. Binzel^a, Francis P. Wilkin^e, Emily A. Mailhot^{f,7}, Alan H. Midkiff^f, April Russell^{g,8,9}, Robert D. Stephens^h, Vincent Gardinerⁱ, Daniel E. Reichart^j, Joshua Haislip^j, Aaron LaCluyze^{i,10}, Raoul Behrend^k and René Roy^l

^aDepartment of Earth, Atmospheric, and Planetary Sciences, Massachusetts Institute of Technology, Rm. 54-424, 77 Massachusetts Avenue, Cambridge, MA 02139, USA

^bDepartment of Astronomy, Whitin Observatory, Wellesley College, 106 Central Street, Wellesley, MA 02481, USA

^cDepartment of Astronomy, Williams College, 880 Main Street, Williamstown, MA 01267, USA

^dDepartment of Physics and Astronomy, Colgate University, 13 Oak Drive, Hamilton, NY 13346, USA

^eDepartment of Physics and Astronomy, Union College, 807 Union Street, Schenectady, NY 12308, USA

^fStar View Hill Education Center, 120 Wasigan Road, Blirstown, NJ 07825, USA

^gDudley Observatory, 107 Nott Terrace, Suite 201, Schenectady, NY 12308, USA

^hSantana Observatory, 11355 Mount Johnson Court, Rancho Cucamonga, CA 91737, USA

ⁱBoambee Observatory, NSW 2452, Australia

^jDepartment of Physics and Astronomy, University of North Carolina, 120 East Cameron Avenue, Chapel Hill, NC 27599, USA

^kGeneva Observatory, CH-1290 Sauverny, Switzerland

^lBlauvac Observatory, 293 Chemin de St Guillaume, 84570 Blauvac, France

ARTICLE INFO

Keywords:
asteroids
asteroids, rotation
photometry

ABSTRACT

An observational study of Koronis family members' spin properties was undertaken with two primary objectives: to reduce selection biases for object rotation period and lightcurve amplitude in the sample of members' known spin vectors, and to better constrain future modeling of spin properties evolution. Here we report rotation lightcurves of nineteen Koronis family members, and derived results that increase the sample of determined spin vectors in the Koronis family to include 34 of the largest 36 family members, completing it to $H \approx 11.3$ ($D \sim 16$ km) for the largest 32 members. The program observations were made during a total of 72 apparitions between 2005–2021, and are reported here along with several earlier unpublished lightcurves. All of the reported data were analyzed together with previously published lightcurves to determine the objects' sidereal rotation periods, spin vector orientations, and convex model shape solutions. The derived distributions of retrograde rotation rates and pole obliquities appear to be qualitatively consistent with outcomes of modification by thermal YORP torques. The distribution of spin rates for the prograde rotators remains narrower than that for the retrograde rotators; in particular, the absence of prograde rotators having periods longer than about 20 h is real, while among the retrograde rotators are several objects having longer periods up to about 65 h. None of the prograde objects newly added to the sample appear to be trapped in an s_6 spin-orbit resonance that is characteristic of most of the largest prograde objects (Vokrouhlický et al., 2003); these smaller objects either could have been trapped previously and have already evolved out, or have experienced spin evolution tracks that did not include the resonance.

1. Introduction

Studies of spin vector orientations among members of asteroid families provide valuable information to constrain models of asteroid spin evolution processes. Members of a family comprise a group of asteroids that were formed together from the outcome of collisional disruption of a parent body, sharing the same physical structure as reaccumulated gravitational aggregates, the same age since formation, and similar evolution for similar lengths of time. Thus family members serve as a constrained sample that avoids difficulties of interpreting a distribution of spin properties which does not share a common origin and dynamical history.

Prior to determinations of thirteen Koronis family members' spin vectors by Slivan et al. (2003, 2009), spin vectors of main belt asteroids smaller than about 40 km had not been much explored, nor had there been a systematic program of spin vector determinations within any particular asteroid family, although statistically larger lightcurve amplitudes of Koronis family asteroids gave an early indication that Koronis family spin vectors might have some preferential alignment (Binzel, 1988, 1990). The markedly non-random distribution of measured spin vectors determined initially from observations of ten of the largest Koronis family members (Slivan, 2002) revealed evidence of modification of their spins by YORP thermal radiation torques, in some cases combined with solar and planetary gravitational torques (Vokrouhlický et al., 2003). The distribution of spin vectors among the previously studied sample is dominated by two groupings: a group of low-obliquity retrograde spins spanning a wide range of periods between about 3 h and 30 h, and a smaller group of prograde spins with obliquities near 45° and periods near 8 h, characteristic of trapping in the s_6 spin-orbit resonance (Vokrouhlický et al., 2003). A single “stray” longer-period, low-obliquity prograde object (Slivan et al., 2009) subsequently was joined by the largest family member (208) Lacrimosa (Vokrouhlický et al., 2021) which initially had been misidentified as being in the retrograde group based on an alias sidereal period.

A limitation of the previously studied Koronis family spin vector sample comprising 13 of the largest 18 family members, as classified by Mothé-Diniz et al. (2005) and using relative catalog absolute magnitudes H from the coincident compilation by Tholen (2009) as a proxy for relative sizes, is that selection biases render that sample complete to only the largest 8 members. Although that set of spin vectors was sufficient to have revealed evidence of YORP modification in the distribution of spin rates and spin obliquities, the small size of the completed sample and the presence of bias effects limit its usefulness for further understanding of the spin evolution. In particular, because the rate at which YORP acts on a body is size-dependent, one may expect systematic study of smaller members of the family to reveal information that is not apparent from the distribution of spin vectors in the incomplete sample of larger members.

Kryszczyńska et al. (2007) noted the need for more spin vector data for family main belt asteroids; subsequently Kryszczyńska (2013) studied spin vectors of 18 members of the Flora family and reported evidence of YORP modification, identifying at least three objects which may be trapped in a so-called “Slivan state” spin-orbit resonance as described by Vokrouhlický et al. (2003). Kim et al. (2014) studied spin vectors of 13 members of the Maria family and did not detect spin vector alignment, but did find evidence of YORP modification of spin rates in a sample of 92 members. Hanuš et al. (2013) investigated anisotropy of spin vectors in eight asteroid families including Koronis, Flora, and Maria, corroborating finding depopulation of poles close to the ecliptic plane, but did not find any candidates for spin-orbit resonance trapping in their 38-member sample from the Flora family. In each of the studies the families' spin vector samples were not controlled for completeness to any particular size.

Obtaining the data needed for a deliberate spin vector determination program represents a considerable observing effort necessarily spanning a number of years. Determination of a spin vector from ground-based lightcurve observations requires that the data set (a) includes observations from a sufficient number of different viewing aspects, (b)

*Corresponding author

slivan@mit.edu (S.M. Slivan)

ORCID(s): 0000-0003-3291-8708 (S.M. Slivan)

¹Present address Univ. of California at Los Angeles, CA, USA

²Present address Dept. of Physics and Astronomy, Univ. of Victoria, BC, Canada

³Present address Dept. of Astronomy, Univ. of Mass. at Amherst, MA, USA

⁴Present address Institute for Astronomy, Univ. of Hawaii, Honolulu, HI, USA

⁵Present address Dept. of Earth and Environment, Boston Univ., MA, USA

⁶Present address Southwest Research Institute, Boulder, CO, USA

⁷Present address Steward Observatory, Univ. of Arizona, Tucson, AZ, USA

⁸Present address John Wiley & Sons, Inc., Hoboken, NJ, USA

⁹Present address Concordia Univ., St. Paul, MN, USA

¹⁰Present address Dept. of Physics, Central Michigan Univ., Mt. Pleasant, MI, USA

spans an interval of time long enough to precisely determine the object's sidereal rotation period, and (c) samples a sufficient progression of shorter time intervals within the long time span to rule out alias sidereal periods. Given that the viewing geometry of a Koronis family member changes very little during any particular apparition, observations from at least five to six apparitions are needed to assemble a suitable lightcurve data set. Slivan et al. (2008) have described a long-term observing program designed and undertaken specifically to obtain the rotation lightcurve data needed to increase the sample of determined Koronis family spin vectors; most of the lightcurves newly reported in the present work were obtained as part of that program.

The new lightcurves, like those used to determine the previously-studied sample of Koronis family spin vectors, would now be characterized as densely-sampled in time in contrast with sparsely-sampled lightcurve data from sky imaging surveys. Several years into the multi-year observing program, Ďurech et al. (2009) independently described a method to exploit the increasing availability of sparse-in-time lightcurves by combining them with a smaller number of densely-sampled lightcurves, provided that the sparse data brightnesses have been calibrated to some common zero-point so that they can be assembled into lightcurves. The availability and quality of sparse data to construct a specific sample of any particular asteroids of interest remain subject to the observing parameters of the sky surveys, including cadence and targeted brightness range. Applications of this “sparse data” approach (Hanuš et al., 2011, 2013; Ďurech et al., 2016, 2018; Ďurech and Hanuš, 2018; Ďurech et al., 2019, 2020) have yielded spin vector determinations for fifteen of the observing program objects; a comparison of those results with spin vectors determined in the present work for the same objects, using the same underlying convex modeling approach and assumptions, but based instead on independent sets of densely-sampled input lightcurves, is included in Sec. 4.

In this paper the lightcurve observations and analyses for spins and convex shape models of nineteen Koronis family members are reported, completing the sample of determined spin vectors in the Koronis family down to $H \approx 11.3$ ($D \sim 16$ km). The results reduce selection biases in the set of known spin vectors for family members, and will constrain future modeling of spin properties evolution; in the meantime, the spin properties in the expanded sample are briefly discussed.

Catalog physical properties for the observing program objects are summarized in Table 1, which lists for each object its catalog absolute magnitude H , available taxonomic classifications, and whether a spectrum has been reported. Taxonomic types have been determined for seventeen of the objects, all of which are classified as either some variety of S-type, or for (1100) Arnica as a union set of two types that includes S-type.

2. Observations

The observing program used CCD imaging cameras at nine different observatories from 2005 September through 2021 August, recording 443 individual rotation lightcurves of the nineteen target objects during 72 different apparitions. Once observations of a target were begun during an apparition, particular efforts were made to obtain complete coverage in rotation phase at a sampling rate of at least 50 points per rotation in order to maximize usefulness of the data for spin vector analyses, and obtaining data to also determine a more precise rotation period was prioritized for objects whose existing period determination was not precise enough to meet the criterion described by Slivan (2012). During most apparitions, observations were made to calibrate the lightcurves to standard magnitudes by observing solar-colored standard stars from Landolt (1983, 1992), and when possible, additional observations were made to increase solar phase angle coverage. Images were processed and measured using standard techniques for synthetic aperture photometry. Also reported here with the observing program data are several previously unpublished lightcurves from one earlier apparition.

Observing circumstances for each object are presented in Table 2, summarized by apparition. The table lists for each apparition the UT date month(s) during which the observations were made, the number of individual lightcurves observed, the approximate ecliptic longitude λ_{PAB} and latitude β_{PAB} (J2000) of the phase angle bisector, the range of solar phase angles α observed, and the filter(s) and telescope used. Information about the telescopes, observatories, and detectors is presented in Table 3. Rotation period results are presented in Table 4, which lists for each object the observed range of peak-to-peak lightcurve amplitudes and the derived periods with their uncertainties. For periods improved during this study the apparition whose lightcurves yield the most precise result is identified. Color index results are summarized in Table 5.

Table 1

Catalog physical properties for the observing program objects.

Asteroid	Catalog H (notes a,b)	Taxonomic classification(s)	Spectrum reported?	Taxonomy reference
(658) Asteria	10.51	S	–	Neese (2010)
(761) Brendelia	10.74	S, SC	–	Neese (2010); Hasselmann et al. (2012)
(811) Nauheima	10.77	S, S0, LS	–	Neese (2010); Hasselmann et al. (2012)
(975) Perseverantia	10.50	S	–	Neese (2010)
(1029) La Plata	10.92	S	–	Neese (2010); Hasselmann et al. (2012)
(1079) Mimosa	11.19	S	–	Neese (2010); Hasselmann et al. (2012)
(1100) Arnica	10.94	LS	–	Hasselmann et al. (2012)
(1245) Calvinia	9.98	S, S0	–	Neese (2010)
(1336) Zeelandia	10.67	S, S0	yes	Neese (2010)
(1350) Rosselia	10.73	S, Sa	yes	Neese (2010)
(1423) Jose	10.97	S	yes	Neese (2010); Hasselmann et al. (2012)
(1482) Sebastiana	11.10	–	–	
(1618) Dawn	11.23	S	yes	Neese (2010)
(1635) Bohrmann	11.08	S	yes	Neese (2010)
(1725) CrAO	11.37	S	yes	Neese (2010)
(1742) Schaifers	11.32	S	–	Hasselmann et al. (2012)
(1848) Delvaux	11.11	S	yes	Neese (2010)
(2144) Marietta	11.35	S	–	Hasselmann et al. (2012)
(2209) Tianjin	11.26	–	–	

^a Catalog H values published in various Minor Planets and Comets Orbit Supplements from the IAU Minor Planet Center, and curated by the Solar System Dynamics group at the NASA Jet Propulsion Laboratory. Retrieved using the JPL Small-Body Database Lookup Web tool https://ssd.jpl.nasa.gov/tools/sbdb_lookup.html on 2022 March 28.

^b Use of catalog H in the present work is limited to serving as proxy for approximate relative sizes of the family members. Solar phase parameters derived from observing program data are reported in Table 6.

Table 2

Summarized observing circumstances.

Object	UT date(s)	N_{lc}	λ_{PAB}	β_{PAB}	α	Filter(s) ^a	Telescope
(658) Asteria	2007 Sep	4	340°	0°	0°–4°	<i>V</i>	b
(761) Brendelia	2005 Sep–Nov	21	353°	–1°	2°–18°	<i>V, R</i>	b
	2006 Dec–2007 Feb	21	90°	+2°	2°–16°	<i>V</i>	b
	2008 Jan–Apr	19	170°	+1°	1°–16°	<i>V, R</i>	b
	2009 May–Jun	9	260°	–2°	3°–9°	<i>V</i>	b,c
	2013 Mar–May	14	183°	+1°	3°–17°	<i>R</i>	b
(811) Nauheima	2005 Dec–2006 Feb	3	98°	–2°	5°–17°	<i>V</i>	b
	2007 Feb–Mar	2	174°	+3°	3°–7°	<i>V</i>	b
(975) Perseverantia	2005 Sep	1	357°	–2°	6°	<i>V</i>	b
	2006 Nov–2007 Feb	6	97°	+3°	6°–19°	<i>V, R</i>	b
	2008 Mar–Apr	4	197°	+1°	3°–9°	<i>V</i>	b
	2013 May	5	218°	0°	2°–6°	<i>R</i>	b
(1029) La Plata	2005 Dec	4	78°	+2°	1°–3°	<i>V</i>	b
	2007 Mar–Apr	4	173°	+2°	1°–15°	<i>V</i>	b
(1079) Mimosa	1984 Nov	5	68°	+2°	1°–4°	<i>B</i>	k
	2013 Oct–Nov	14	43°	+1°	1°–13°	<i>R</i>	b
	2016 Apr–May	8	235°	–1°	1°–7°	<i>R</i>	l
	2017 Jul–Aug	11	319°	0°	2°–8°	<i>R</i>	l
	2021 May–Jul	30	247°	–1°	6°–18°	<i>r', R</i>	m,n
(1100) Arnica	2007 Sep–Nov	7	20°	+1°	1°–12°	<i>V, R</i>	b
	2009 Jan–Mar	9	111°	0°	3°–18°	<i>V, R</i>	b
	2010 Feb–Apr	7	188°	–1°	2°–12°	<i>c</i>	d
	2011 May–Jun	6	279°	–1°	3°–14°	<i>V</i>	c,e
	2012 Sep–2013 Jan	6	32°	+1°	1°–20°	<i>V, R</i>	b
	2014 Jan	5	115°	0°	2°–6°	<i>R</i>	b
(1245) Calvinia	2006 Jul	3	269°	+3°	9°–13°	<i>V</i>	b
	2007 Oct	1	15°	–3°	4°	<i>V</i>	b
	2012 Dec	1	26°	–3°	17°	<i>V</i>	b
(1336) Zeelandia	2006 Oct	5	335°	–4°	14°–20°	<i>V, R</i>	b
	2007 Nov–Dec	2	72°	–2°	2°	<i>V</i>	b
	2009 Mar–Apr	3	155°	+3°	7°–17°	<i>V, R</i>	b
	2010 Jun	5	245°	+2°	4°–7°	<i>V</i>	c
	2011 Aug–Oct	6	352°	–4°	8°–14°	<i>V</i>	e
	2013 Jan–Mar	4	91°	0°	8°–19°	<i>R</i>	b
	2014 Mar–Apr	6	170°	+4°	7°–14°	<i>R</i>	b
(1350) Rosselia	2006 Sep	3	335°	–1°	6°–10°	<i>V, R</i>	b
	2007 Dec	2	89°	–3°	1°–2°	<i>V</i>	b
(1423) Jose	2006 Jan–Mar	6	139°	+4°	4°–14°	<i>V</i>	b
	2007 Apr–Jun	7	218°	+1°	2°–14°	<i>V</i>	b,f
(1482) Sebastiana	2006 Mar–Apr	4	151°	+4°	5°–18°	<i>V</i>	b
	2007 May–Jun	4	244°	0°	1°–9°	<i>V</i>	b
(1618) Dawn	2014 Jan	5	99°	0°	3°–12°	<i>R</i>	b
	2015 Feb–Apr	11	187°	+4°	2°–15°	<i>R</i>	b
	2017 Oct–Dec	9	25°	–4°	2°–18°	<i>R</i>	b
	2020 Jun	4	205°	+3°	20°	<i>R</i>	i
	2021 Jun–Aug	12	299°	–1°	3°–15°	<i>R</i>	m

Table 2 (*continued*)

Object	UT date(s)	N_{lc}	λ_{PAB}	β_{PAB}	α	Filter(s) ^a	Telescope
(1635) Bohrmann	2007 Jul–Aug	6	273°	+2°	11°–18°	<i>R</i>	b
	2008 Oct–Nov	10	20°	−1°	1°–14°	<i>V, R</i>	b
	2009 Nov–2010 Feb	6	110°	−2°	3°–15°	<i>V, R</i>	b,d,g
	2011 Apr–May	3	192°	+1°	8°–11°	<i>c</i>	d
	2012 Jun–Jul	6	290°	+2°	1°–11°	<i>V, R</i>	b,c
(1725) CrAO	2014 Sep–Oct	8	353°	−3°	3°–16°	<i>V, r'</i>	b
	2016 Jan–Feb	5	95°	−1°	7°–15°	<i>V, R</i>	b
	2017 Mar–Apr	7	171°	+3°	4°–15°	<i>R</i>	b
	2018 Jul–Aug	5	253°	+2°	16°–20°	<i>R</i>	h
	2019 Aug	3	356°	−3°	10°–13°	<i>R</i>	h
(1742) Schaifers	2007 Jul–Aug	6	289°	+2°	2°–9°	<i>R</i>	b
	2013 Oct–2014 Feb	12	51°	−3°	2°–21°	<i>V, R</i>	b
	2015 Feb	2	142°	−1°	1°–4°	<i>R</i>	b
	2016 Apr–May	2	217°	+3°	1°–5°	<i>R</i>	b
(1848) Delvaux	2006 Nov–Dec	2	336°	0°	20°	<i>R</i>	b
	2009 Mar–Apr	2	152°	0°	10°–14°	<i>V, R</i>	b
	2013 Feb	1	79°	+2°	18°	<i>R</i>	b
	2014 Apr	2	164°	−1°	15°–17°	<i>R</i>	b
	2015 Jun	1	259°	−2°	6°	<i>R</i>	j
(2144) Marietta	2007 Oct–Nov	4	28°	−3°	2°–9°	<i>V</i>	b
	2015 Mar–Jun	3	230°	+4°	10°–15°	<i>R</i>	b
	2016 Aug	1	313°	0°	1°	<i>R</i>	b
(2209) Tianjin	2007 Nov–Dec	4	57°	−3°	4°–10°	<i>V</i>	b
	2009 Apr	6	162°	+1°	15°–18°	<i>V, R</i>	b
	2013 Feb–Apr	5	89°	−2°	20°–21°	<i>R</i>	b
	2014 Mar–Apr	6	178°	+2°	4°–12°	<i>R</i>	b
	2016 Sep	2	351°	−1°	4°–5°	<i>R</i>	b

^a Filters: *B*, Johnson *B*; *V*, Johnson *V*; *R*, Cousins *R*; *r'*, SDSS *r'*; *c*, colorless.

^b 0.6-m Sawyer, Whitin Obs., observers S. Slivan and Corps of Loyal Observers, Wellesley Division (CLOWD)

^c 0.4-m PROMPT, CTIO, observers S. Slivan, and in 2009 M. Hosek

^d 0.35-m, Santana Obs., observer R. Stephens

^e 0.32-m GRAS-009, Siding Spring Obs., observer A. Russell

^f 0.3-m, Boambee Obs., observer V. Gardiner

^g 0.6-m, Hopkins Obs., observer M. Hosek

^h 0.6-m Elliot, Wallace Obs., observer S. Slivan

ⁱ 0.6-m Elliot, Wallace Obs., observer T. Brothers

^j 0.6-m, Star View Hill Education Center, observers E. Mailhot and A. Midkiff

^k 0.91-m, McDonald Obs., observer R. Binzel

^l 0.43-m T17, Siding Spring Obs., observer S. Slivan

^m 0.36-m C14 #3, Wallace Obs., observers A. Colclasure, I. Escobedo, A. Henopp, R. Knight, A. Mitchell

ⁿ 0.6-m CHI-1, El Sauce Obs., observer F. Wilkin

Table 3

Telescopes, observatories, detectors.

Telescope	Location	Detector field of view (')	Image resolution ("/pix)	Note
0.61-m Sawyer	Whitin Obs., Wellesley, MA (2005–2009)	16 × 16	1.8	a
0.61-m Sawyer	Whitin Obs., Wellesley, MA (2012–2016 Feb)	19 × 19	1.2	a
0.61-m Sawyer	Whitin Obs., Wellesley, MA (2016 Apr–May)	16 × 16	0.9	a
0.61-m Sawyer	Whitin Obs., Wellesley, MA (2016 Aug–2017 Apr)	19 × 19	1.2	a
0.61-m Sawyer	Whitin Obs., Wellesley, MA (2017 Oct–Nov)	16 × 16	0.9	a
0.61-m Sawyer	Whitin Obs., Wellesley, MA (2017 Dec)	20 × 20	1.2	a
0.4-m PROMPT	Cerro Tololo Inter-American Obs., Chile	10 × 10	0.6	a
0.61-m Elliot	Wallace Astrophysical Obs., Westford, MA	32 × 32	0.9	a
0.36-m C14 #3	Wallace Astrophysical Obs., Westford, MA	20 × 20	1.2	a
0.35-m	Santana Obs., Rancho Cucamonga, CA	21 × 21	1.2	b
0.43-m T17	Siding Spring Obs., Australia	16 × 16	0.9	a
0.32-m GRAS009	Siding Spring Obs., Australia	27 × 18	0.7	b
0.6-m CHI-1	El Sauce Obs., Rio Hurtado, Chile	32 × 32	1.2	a
0.6-m	Hopkins Obs., Williamstown, MA	21 × 21	1.2	a
0.6-m	Star View Hill Obs., Blairstown, NJ	11 × 11	2.6	b,c
0.3-m	Boambee Obs., New South Wales, Australia	24 × 16	1.9	
0.91-m	McDonald Obs., Ft. Davis, TX	–	–	d

^a Observing and data reduction procedures as previously described by Slivan et al. (2008).

^b Images measured using the “Canopus” application developed by B. Warner, Palmer Divide Obs., Colorado Springs, CO.

^c Equipment and procedures described by Mailhot and Midkiff (2014).

^d Photometric photomultiplier tube detector; equipment and procedures described by Binzel (1987).

Solar phase parameters derived from single apparitions using the approach described by Slivan et al. (2008) are summarized in Table 6. The table lists for each solar phase fit result the object and apparition, the span of solar phase angles fitted, the broadband filter used, and the corresponding H and G values, where parentheses around the latter indicate that G was adopted rather than fitted. Absolute magnitudes H were determined only from apparitions during which standard-calibrated lightcurve observations were made at phase angles of 2° or smaller. Fitted values of the slope parameter G were determined only for apparitions whose observations also span at least seven degrees of phase angle within the approximately linear part of the brightness model, at phase angles larger than 5° ; otherwise, a value for G was adopted and held fixed while fitting for the corresponding H value. Adopted G values were calculated from existing fitted values in Slivan et al. (2008) and in the present paper when at least one such value is available; otherwise, they are assigned the value 0.23 ± 0.11 (Lagerkvist and Magnusson, 1990).

Selected plots of composite lightcurves from the observing program are arranged by apparition in Fig. 1; the complete data will be made available online. The time axis on each plot is marked in UT hours on the composite date, showing one cycle of the rotation period plus the earliest and latest 10% repeated. Individual nights’ data have been corrected for light-time and folded using the given period; the legend identifies the UT dates of the original observations. Each graph shares a uniform brightness axis scale spanning 1.0 magnitude. Standard-calibrated brightnesses have been reduced for changing distances and solar phase angles; relative brightnesses were composited by shifting in brightness for best fit to the composite.

Table 4

Lightcurve amplitude and rotation period results.

Asteroid	Amplitude (mag.)	Period P (h)	$\sigma(P)$	Period apparition or reference
(658) Asteria	0.19–0.23	21.032	0.004	Slivan et al. (2008)
(761) Brendelia	0.15–0.36	58.00	0.02	2013
(811) Nauheima	0.03–0.17	4.0011	0.0003	Slivan et al. (2008)
(975) Perseverantia	0.11–0.25	7.224	0.001	Slivan et al. (2008)
(1029) La Plata	0.15–0.56	15.310	0.002	Slivan et al. (2008)
(1079) Mimosa	0.06–0.33	64.69	0.05	2021
(1100) Arnica	0.01–0.30	14.533	0.002	2012–2013
(1245) Calvinia	0.18–0.40	4.8512	0.0003	Slivan et al. (2008)
(1336) Zeelandia	0.01–0.51	15.602	0.002	Slivan et al. (2008)
(1350) Rosselia	0.43–0.54	8.140	0.001	Slivan et al. (2008)
(1423) Jose	0.60–0.73	12.3125	0.0008	2006
(1482) Sebastiana	0.50–0.83	10.489	0.002	Slivan et al. (2008)
(1618) Dawn	0.27–0.78	43.204	0.012	2015
(1635) Bohrmann	0.01–0.51	5.8643	0.0003	2009–2010
(1725) CrAO	0.07–0.26	21.475	0.006	2014
(1742) Schaifers	0.61–0.95	8.533	0.001	Slivan et al. (2008)
(1848) Delvaux	0.52–0.81	3.6391	0.0002	2014
(2144) Marietta	0.29–0.49	5.4889	0.0003	2015
(2209) Tianjin	0.23–0.56	9.4529	0.0007	2012–2013

Table 5

Color index results.

Asteroid	$V-R$	$\sigma(V-R)$	$r'-R$	$\sigma(r'-R)$
(761) Brendelia	0.454	0.017	–	–
(1079) Mimosa	–	–	0.244	0.006
(1100) Arnica	0.451	0.017	–	–
(1336) Zeelandia	0.432	0.023	–	–
(1350) Rosselia	0.466	0.018	–	–
(1635) Bohrmann	0.452	0.023	–	–
(1725) CrAO	0.462	0.027	–	–
(1742) Schaifers	0.440	0.015	–	–
(1848) Delvaux	0.452	0.020	–	–
(2209) Tianjin	0.443	0.035	–	–

Table 6
Solar phase results.

Asteroid	Apparition	Phase angles fitted	Filter	H	$\sigma(H)$	G	$\sigma(G)$
(658) Asteria	2007	0°–4°	V	10.47	0.01	(0.17) ^a	(0.01)
(761) Brendelia	2005	2°–18°	R	10.36	0.02	0.29	0.01
	2006–2007	2°–16°	V	10.82	0.02	0.23	0.01
	2008	1°–15°	V	10.83	0.02	0.27	0.01
(1029) La Plata	2005	1°–3°	V	10.79	0.01	(0.16) ^a	(0.03)
	2007	1°–15°	V	11.02	0.03	0.14	0.01
(1079) Mimosa	1984	1°–4°	B	12.11	0.03	(0.24) ^a	(0.01)
	2013	1°–13°	R	10.88	0.03	0.25	0.02
	2016	1°–7°	R	10.92	0.05	(0.24) ^a	(0.01)
	2017	2°–8°	R	10.72	0.03	(0.24) ^a	(0.01)
(1100) Arnica	2007	1°	R	10.72	0.02	(0.23) ^b	(0.11)
	2012–2013	1°–2°	R	10.78	0.03	(0.23) ^b	(0.11)
	2014	2°–4°	R	10.39	0.04	(0.23) ^b	(0.11)
(1336) Zeelandia	2007	2°	V	10.70	0.01	(0.20) ^a	(0.01)
(1350) Rosselia	2007	2°	V	10.78	0.03	(0.23) ^b	(0.11)
(1423) Jose	2007	2°–4°	V	11.04	0.02	(0.15) ^a	(0.03)
(1482) Sebastiana	2007	1°–5°	V	11.15	0.02	(0.20) ^a	(0.02)
(1618) Dawn	2015	2°–15°	R	10.88	0.04	0.22	0.02
(1635) Bohrmann	2008	1°–14°	V	11.02	0.02	0.29	0.01
	2012	1°–2°	V	11.27	0.02	(0.24) ^a	(0.07)
(1742) Schaifers	2007	2°–4°	R	10.97	0.02	(0.17) ^a	(0.02)
	2013	2°–16°	R	10.85	0.03	0.17	0.02
	2015	1°–4°	R	10.87	0.01	(0.17) ^a	(0.02)
	2016	1°–5°	R	10.89	0.01	(0.17) ^a	(0.02)
(1848) Delvaux	2014 ^c	1°–4°	R	10.73	0.03	(0.23) ^b	(0.11)
(2144) Marietta	2007	2°–4°	V	11.40	0.03	(0.23) ^b	(0.11)
	2016	1°	R	10.90	0.02	(0.23) ^b	(0.11)

^a Adopted G by combining the fitted values available for this object from this work and from Slivan et al. (2008, Table 3).

^b Adopted G from Lagerkvist and Magnusson (1990).

^c (1848) Delvaux lightcurves from Arredondo et al. (2014).

Spin vectors in the Koronis family: IV.

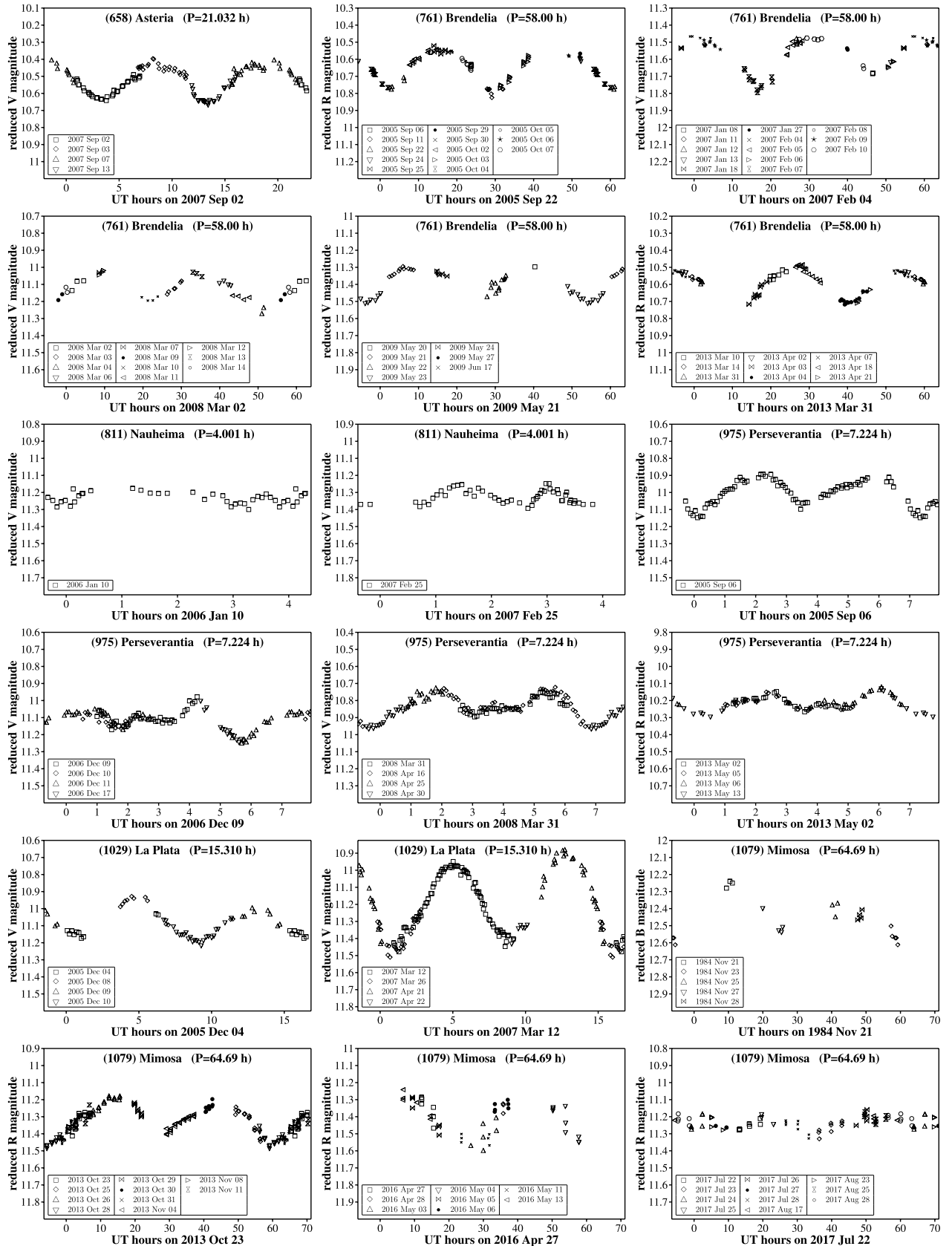
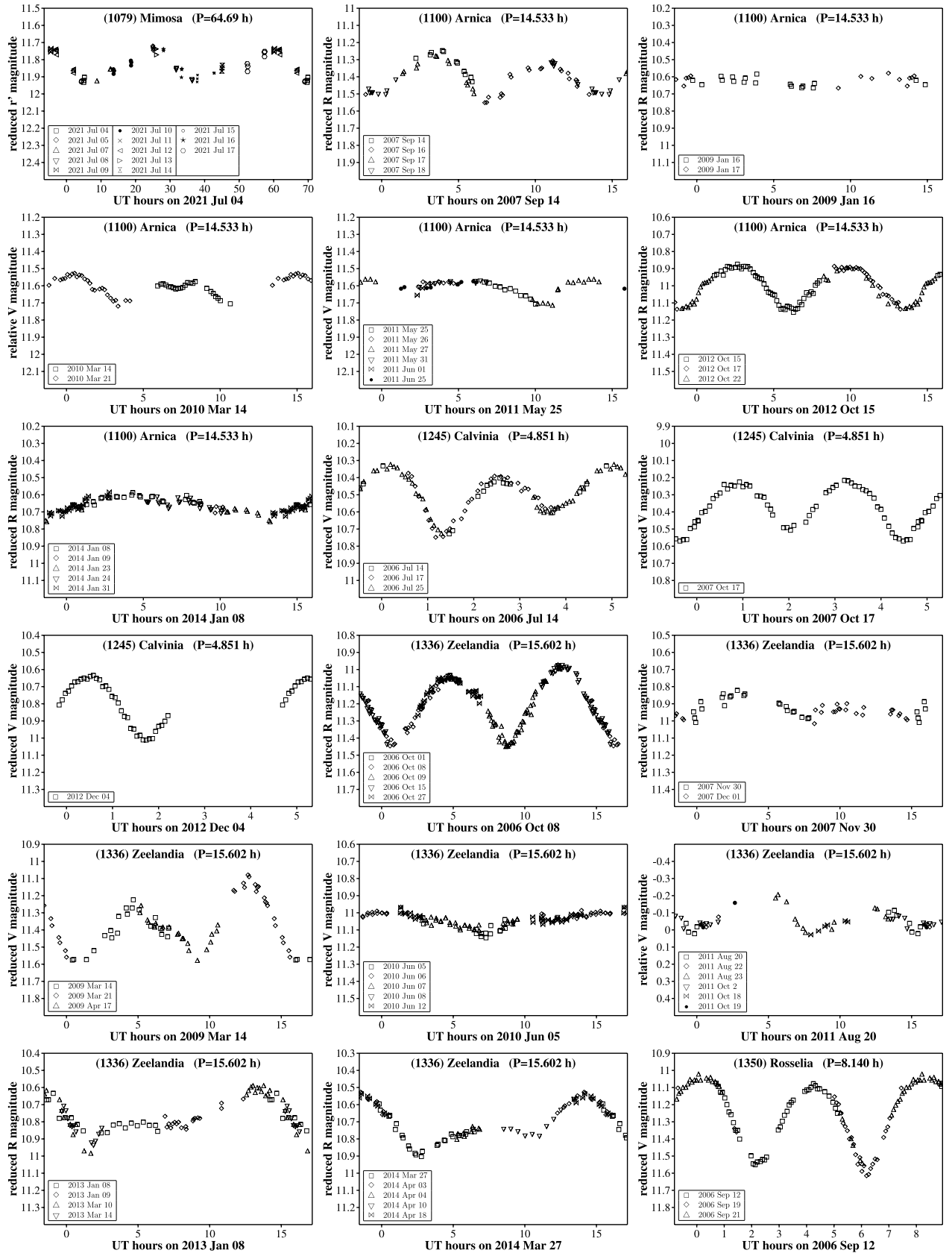


Figure 1: Selected composite rotation lightcurves by object and apparition.

Spin vectors in the Koronis family: IV.



(Fig. 1 continued)

Spin vectors in the Koronis family: IV.

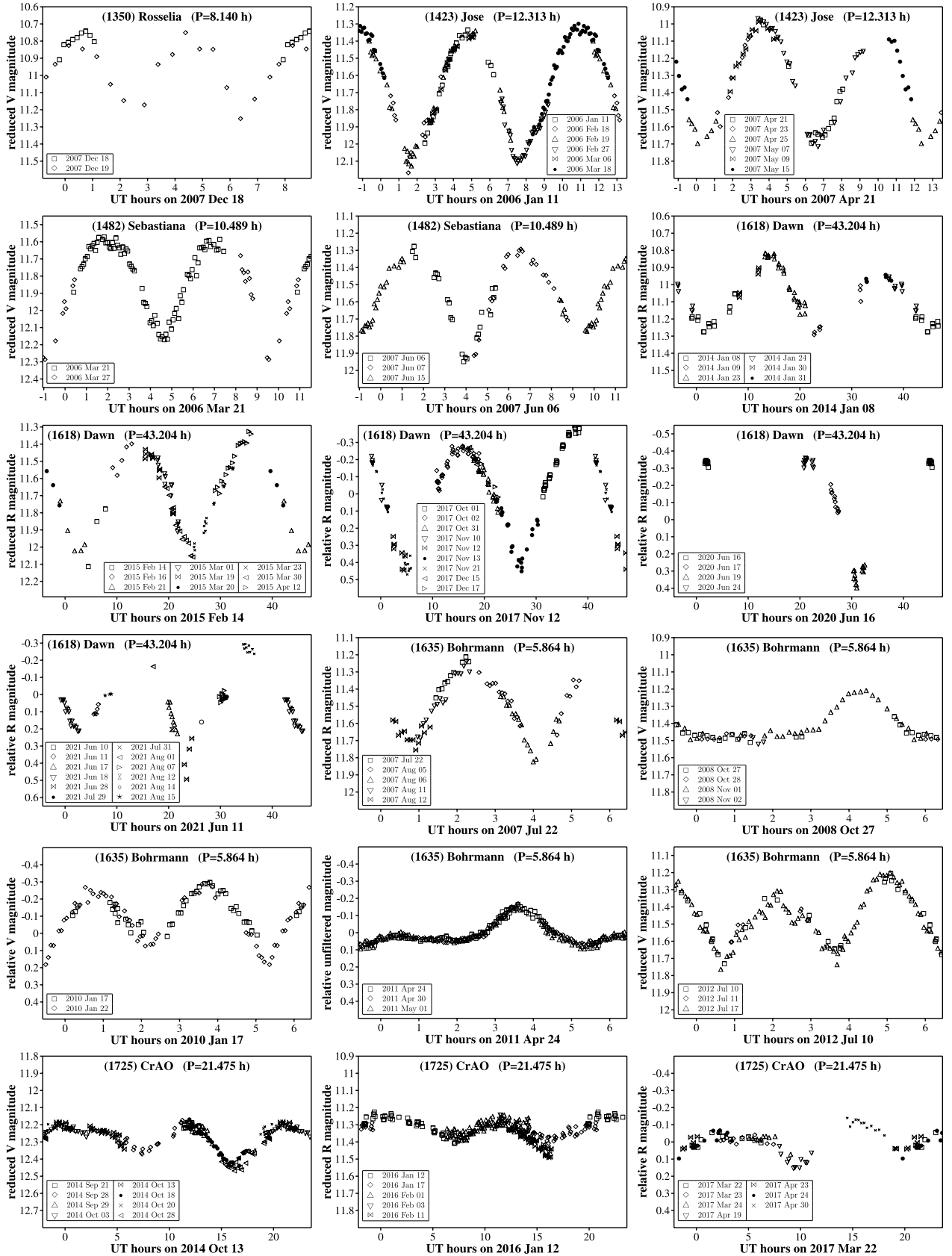


(Fig. 1 continued)

Spin vectors in the Koronis family: IV.

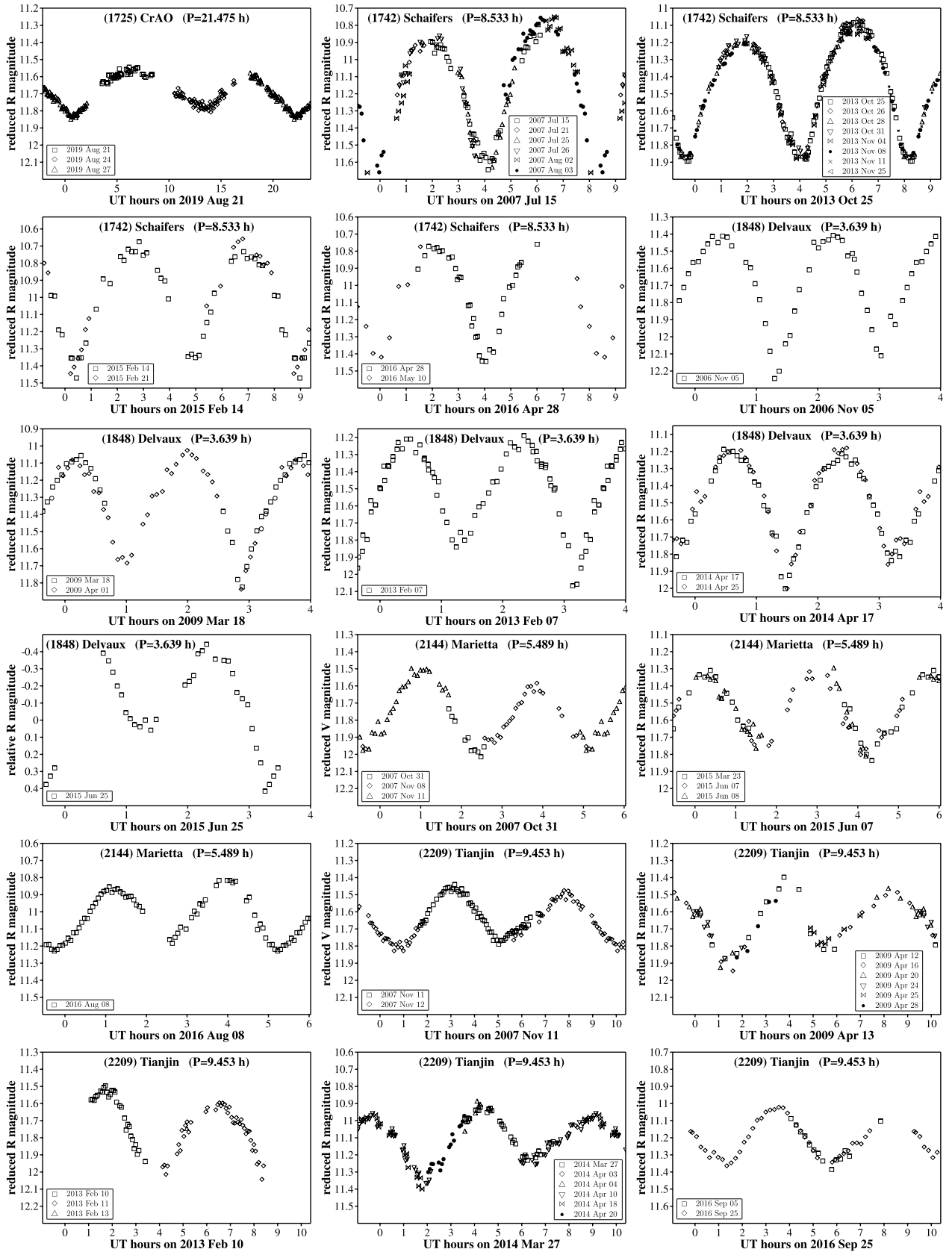


(Fig. 1 continued)

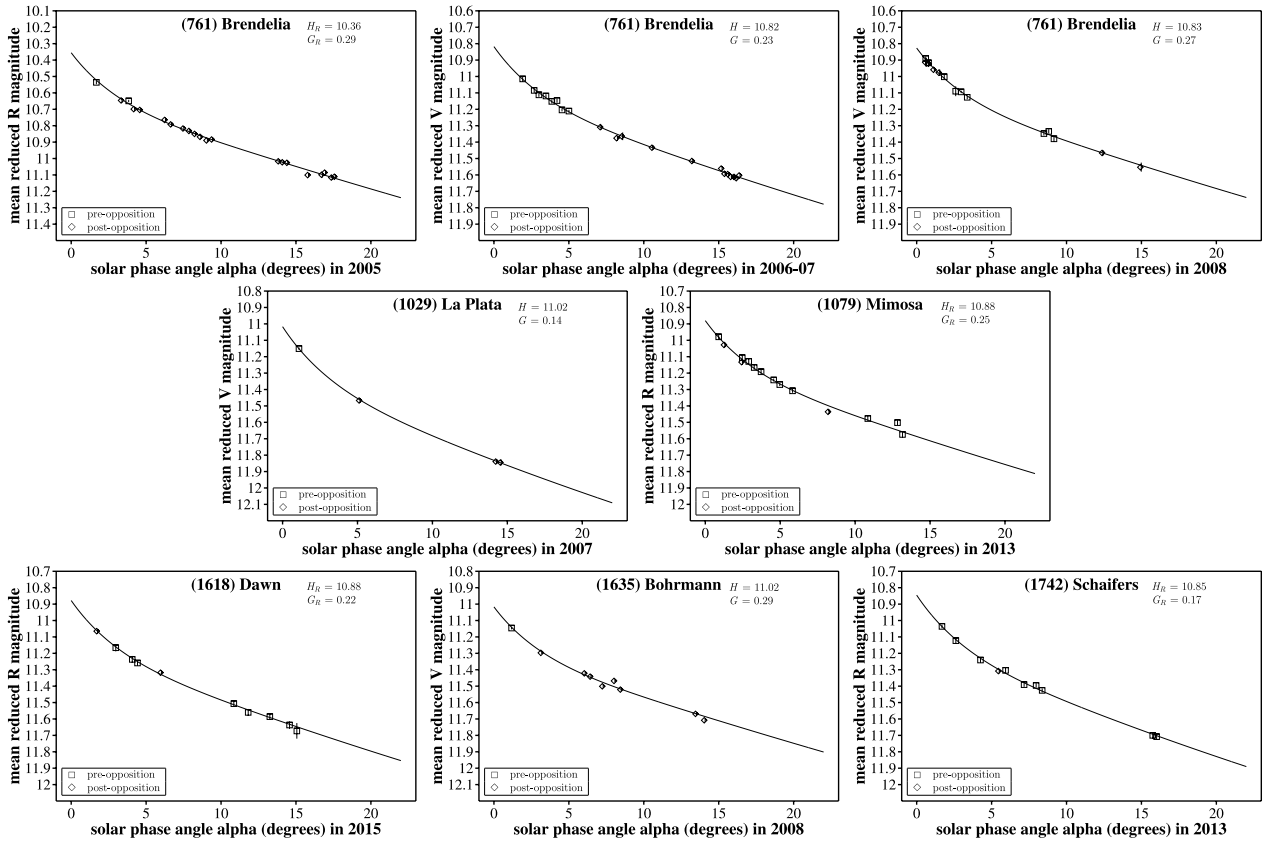


Figure 2: Single-apparition solar phase curves.

Solar phase curves corresponding to the eight apparitions yielding fitted values for the slope parameter G are shown in Fig. 2, in which mean reduced magnitudes are plotted as a function of phase angle. On each graph the solid curve represents the best fit of the Lumme-Bowell phase function (Bowell et al., 1989) to the mean brightnesses; the corresponding H and G values appear in the upper right-hand corner of the plot.

2.1. Notes on individual objects' lightcurves

(811) *Nauheima*. The lightcurves recorded during both of the apparitions reported here exhibit significant shape changes over the periods of the observations.

(1079) *Mimosa*. A previously unpublished lightcurve recorded in 1984 during the observing program of Binzel (1987) also is reported here.

(1100) *Arnica*. Slivan et al. (2008) observed lightcurves from low-amplitude viewing aspects and initially deduced a rotation period that is double the correct value, and in a note added in proof also reported the correct period based on additional lightcurves that were recorded in 2007; those doubly-periodic observations are fully reported here. The $V-R$ color index reported in Table 5 is the weighted mean of independent measurements made during the 2009 and the 2012–13 apparitions.

(1336) *Zealandia*. The $V-R$ color index reported in Table 5 agrees with the measurement by Thomas et al. (2011) of 0.431 ± 0.021 .

(1848) *Delvaux*. Arredondo et al. (2014) reported lightcurves from the 2014 apparition spanning 18 days. Additional observations made later in the same apparition on two more nights are reported here, which extend the observed time span to 61 days and were used to determine the synodic rotation period in Table 4.

3. Analysis for sidereal periods, spin vectors, and model shapes

The spin vector and model shape analyses were carried out as a sequence of five identifiable stages, as described in this section: resolving the sidereal rotation count, determining the sidereal period and direction of spin, resolving the locations of the symmetric pair of pole regions, determining the best-fit spin vectors and a preliminary model shape, and finally fitting a refined model shape for presentation. A comprehensive discussion of the analysis method is presented as well as are details of its application to particular objects, not only to share the basis for confidence in the final results presented, but also as an aid and reference for those who may wish to perform their own spin vector and model shape analyses of lightcurves, mindful that only limited such information has made its way into the literature since the introduction of the convex inversion method (Kaasalainen and Torppa, 2001; Kaasalainen et al., 2001).

Sidereal period and direction of spin. A prerequisite for a correct spin vector analysis is correctly counting the number of rotations that elapsed during the entire span of the lightcurve observations, in order to determine the correct sidereal rotation period. In that context, discussion of both the synodic period constraint and the sampling of a progression of time intervals between epochs can be found in Slivan (2012, 2013). Each program object's sidereal period was constrained based on analysis of epochs that were determined from the lightcurves composited by apparition, using a Fourier series filtering approach to identify information related to low-order object shape. Most of the program objects' apparitions' lightcurves are doubly periodic and relatively symmetric with sufficient amplitude to make measuring the epochs straightforward. The synodic rotation period from Table 4 was used to fit a Fourier series model, choosing an appropriate number of up to eight harmonics based on the sampling of the data, then filtered for low-order shape by retaining only the second harmonic to locate times of lightcurve maxima. Epoch errors were estimated as $1.5\times$ the larger of either the time difference between the corresponding filtered and unfiltered maxima, or 1% of the rotation period which is on the order of the typical RMS error of a well-determined fit to epochs.

Composite lightcurves having a gap in coverage longer than 1/4-rotation are too incomplete to use a doubly-periodic model; in those cases a singly-periodic model at half the rotation period was fit instead and then filtered for the fundamental. In a few cases, lightcurves having the lowest amplitudes or the greatest departures from doubly-periodic symmetry required special attention to locate epochs and are discussed with the objects' analyses. Epochs estimated from incomplete or low-amplitude lightcurves were assigned relatively larger uncertainties.

In the first stage of the epochs analysis for each object, the "sieve algorithm" of Slivan (2013) was used with the synodic rotation periods in Table 4 to identify possible sidereal rotation counts, and their corresponding range(s) of possible sidereal periods, that are consistent with the filtered epochs. For all but one of the program objects the sieve algorithm by itself yielded a single candidate sidereal rotation count, leaving only the direction of spin unknown. Then in the second stage each candidate period, prograde and retrograde, was checked as described by Slivan (2014), using the epochs with Sidereal Photometric Astrometry (SPA) (Drummond et al., 1988) to identify the sidereal period, direction of spin, and a first indication of either a single pair of symmetric pole solution regions or a single merged region at an ecliptic pole. An individual example of pole regions located by SPA is presented as Fig. 3.

The remaining stages of analysis use the convex inversion (CI) method of Kaasalainen et al. (2001), a nonlinear iterative approach. The `convexinv` implementation¹ by J. Ďurech was used, guided by its accompanying documentation when choosing most of its run-time parameter settings. An exception is that for setting the zero time t_0 and initial ellipsoid orientation angle ϕ_0 the suggestion of Kaasalainen et al. (2001) was followed instead, choosing values that align the long axis of the model shape along the x -axis. Doing so avoids very large adjustments to the model during the first several fit iterations which can distort the ultimate outcome. Thus t_0 was set to be the time of a brightness minimum from the filtered Fourier series for a lightcurve recorded at among the smallest available solar phase angles, and then ϕ_0 was calculated as the corresponding pole-dependent astero-centric longitude of the sub-PAB point (Taylor, 1979; Slivan, 2014, Eqs. 3–8) based on the initial value supplied for the pole location. The distribution code also was modified to support user-specified values for the axial ratios of the triaxial ellipsoid used as the initial model shape, and the initial value for a/b generally was selected based on the maximum amplitude from among the Fourier series-filtered observed lightcurves.

The lightcurve data were binned to a bin width of 1/50 of the rotation period for the CI analyses. Data sets were analyzed as relative photometry, except for the three longest-rotation period objects (761) Brendelia, (1079) Mimosa, and (1618) Dawn whose single-night lightcurves, even from the longest observing nights, individually do not record enough of a rotation to determine the shape of the lightcurve without referencing brightnesses on different nights to a common zero point. To prepare these objects' data sets for CI, data whose brightnesses had been calibrated to standard

¹https://astro.troja.mff.cuni.cz/projects/damit/pages/software_download

Spin vectors in the Koronis family: IV.

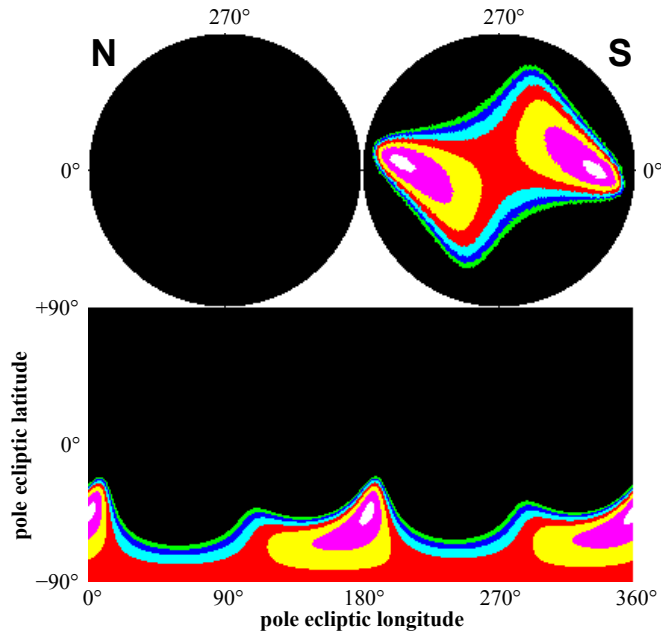


Figure 3: Example contour graph of RMS fit errors using SPA for trial pole “scans” for program object (1635) Bohrmann, showing the entire celestial sphere in ecliptic coordinates plotted in both polar and rectangular formats, with areas of best-fit poles colored white. In this case the locations of the pair of broader pole regions entirely in the south ecliptic hemisphere indicate retrograde rotation.

stars were referenced to a common zero-point by using available color index information, and solar phase function coefficients were included as fitted parameters for CI analysis of these lightcurves as standard-calibrated photometry. Lightcurves for these longer-period objects whose individual nights had been referenced to the same comparison star but *not* also put onto a standard system, instead were composited in time and in brightness into “preassembled” lightcurves of relative photometry.

Pole regions. For the third stage of the analyses, a contour graph of CI model fits’ χ^2 goodness-of-fit value as a function of pole location was constructed to identify the pole regions. Using the known sidereal period, a series of CI trials were run on a grid pattern of trial pole coordinates having 2° -resolution in latitude and longitude to systematically cover the ecliptic hemisphere indicated by SPA, in each case holding the pole fixed at the trial location and iterating until the step change in the RMS deviation decreased to less than 0.001. It was found that the pole region location results were relatively insensitive to weighting of the lightcurves. An individual example of pole regions located by CI is presented as Fig. 4.

Although pole regions also already are available from the epochs analysis, the program objects data sets’ are large enough to expect that the CI region locations will be more reliable, because SPA pole longitudes can be subject to systematic errors depending on the degree to which the epochs depart from the assumption that they all correspond to the same asteroid-centric longitude. The SPA region results did prove useful, however, to distinguish the correct solutions when CI allowed more than one possible pair of pole regions. The remaining symmetric pole ambiguity for the program objects cannot be resolved using Earth-based lightcurves, because these asteroids all share low orbital inclinations of 1 to 3 degrees as members of the Koronis family. A discussion of symmetry and ambiguities pertinent to pole solutions obtained from lightcurves can be found in Magnusson et al. (1989).

Spin poles. In the fourth stage CI was run to determine a best-fit period, pole, and preliminary possible model shape, using the initial period from SPA and an initial pole location estimated from the CI contour graph. For the benefit mainly of the preliminary shape model a final version of the binned lightcurve data input was constructed, weighted typically so that the number of fitted data points per apparition is proportional to its available rotation phase coverage, to within a factor of about 1.5. Any process adjustments needed for a particular object are described in its individual notes.

Spin vectors in the Koronis family: IV.

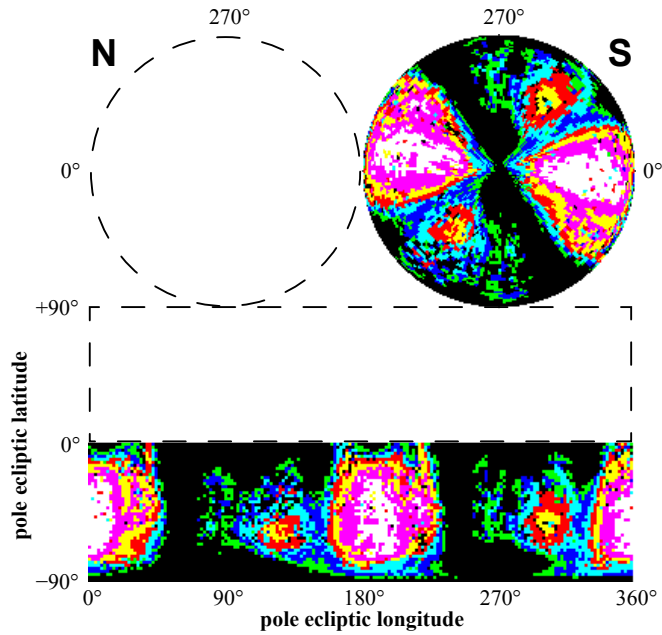


Figure 4: Similar to Fig. 3 but using CI and calculated only for trial poles in the southern ecliptic hemisphere. The pair of pole region locations favored by the lowest χ^2 values agrees with those of the SPA regions.

For these runs of CI, the criterion for stopping the fit iterations was given more deliberate consideration than was for the earlier runs to generate the pole regions contour map. As an aid in determining at what point to stop the fitting, the distribution code was modified to add to the fit iteration log at each step the fractional change in the χ^2 goodness-of-fit metric, and the current sidereal period and pole coordinates. It was found that convergence of the period and pole were straightforward for these data sets, but how much longer to keep adjusting the model shape after the period and pole had converged was not as clear-cut and remained somewhat subjective; analyses of certain data sets showed indications that overfitting could be an issue. The guideline ultimately adopted was to iterate past period and pole convergence only until the step change in the fit relative χ^2 decreased to less than about 0.5%.

Each preliminary model shape result was checked for consistency with an assumption of stable rotation about its shortest axis, by constructing the corresponding model shape rendering and confirming that its shortest dimension lies along the polar axis. To solve for the shape model convex polyhedron from its facet areas and normals, a C translation of the FORTRAN code for Minkowski minimization from the CI distribution was used.

The expected symmetry of an object's two ambiguous pole solutions with respect to the "photometric great circle" (PGC) (Magnusson et al., 1989) was used to perform a self-consistency check on each pair of derived pole solutions, as a significant departure from symmetry would indicate the presence of some problem with the analysis. Appendix A details how symmetric poles were calculated using objects' orbit elements.

Errors were estimated after a solution had passed both consistency checks. The period error was estimated from SPA with the full set of Fourier-filtered epochs for a pole at the adopted location. Uncertainties for the pole locations were estimated from the CI model fits' χ^2 distributions in each case by identifying a constant- χ^2 contour that encloses a region just large enough to entirely surround the insignificant fluctuations near the pole location within an approximately oval-shaped region. The contour's angular extents in ecliptic latitude and longitude were adopted as coarse estimates of $\sim 2\sigma$ confidence, and each error was rounded to the nearest multiple of 5° of arc. The factor of ~ 2 relationship between the subjective identification of contours and the estimated error is based on comparison of the published CI pole error estimates of previously-studied objects (Slivan et al., 2003, 2009) with their CI model fits' χ^2 distributions.

Model shape and axial ratios. In the last stage of the analysis, the final shape renderings and axial ratios corresponding to the best-fit period and pole results were obtained using the `conjgradinv` implementation from

the CI distribution, which uses the facet areas directly rather than using spherical harmonics. The axial ratios for its initial ellipsoid were estimated from the preliminary model shape.

3.1. Spin and shape results

The lightcurves reported in Sec. 2 were combined with lightcurves of the program objects previously published by Slivan et al. (2008) (46 apparitions) and by Binzel (1987) (6 apparitions), plus lightcurves from 10 more apparitions whose sources are given in the analysis descriptions for their specific objects. Table 7 summarizes for each asteroid's available combined lightcurve data set the span of years included, the number of apparitions N_{ap} , and aspect information as a list of ecliptic longitudes λ_{PAB} of the asteroids' phase angle bisector (PAB) near the mid-date of the observations from each apparition.

Table 7
Summary of lightcurve observations used for spin vector analyses.

Asteroid	Years observed	N_{ap}	λ_{PAB} of aspects observed ($^{\circ}$)
(658) Asteria	1983–2007	6	53, 68, 167, 323, 340, 352
(761) Brendelia	2001–2013	7	75, 90, 158, 170, 183, 260, 353
(811) Nauheima	1984–2007	7	9, 98, 174, 239, 253, 340, 347
(975) Perseverantia	1990–2013	8	74, 97, 176, 197, 218, 267, 296, 357
(1029) La Plata	1975–2007	7	32, 78, 141, 173, 228, 328, 350
(1079) Mimosa	1983–2021	8	20, 43, 68, 120, 235, 247, 319, 329
(1100) Arnica	1999–2014	9	20, 32, 99, 104, 111, 115, 183, 188, 279
(1245) Calvinia	1977–2012	7	8, 15, 26, 107, 186, 269, 323
(1336) Zeelandia	1999–2014	9	72, 91, 125, 140, 155, 170, 245, 335, 352
(1350) Rosselia	1975–2007	8	72, 89, 149, 162, 162, 240, 284, 335
(1423) Jose	2002–2007	5	41, 139, 206, 218, 290
(1482) Sebastiana	1984–2007	7	19, 66, 151, 230, 244, 319, 333
(1618) Dawn	2003–2021	6	25, 75, 99, 187, 205, 299
(1635) Bohrmann	2003–2012	7	1, 20, 95, 110, 192, 273, 290
(1725) CrAO	2003–2019	7	95, 171, 236, 253, 341, 353, 356
(1742) Schaifers	1983–2016	7	32, 51, 129, 142, 217, 289, 350
(1848) Delvaux	2004–2015	7	79, 140, 152, 164, 259, 336, 349
(2144) Marietta	1999–2016	7	28, 108, 120, 145, 220, 230, 313
(2209) Tianjin	1996–2016	6	57, 89, 162, 178, 278, 351

The spin vector results for the program objects are presented in Table 8. The first three columns list the asteroid, its derived sidereal period P_{sid} , and its period error. The symmetric pair of pole solutions is given in the next two groups of three columns, each grouped as a pole identifier followed by its J2000 ecliptic coordinates $(\lambda_0; \beta_0)$. For convenient reference the pole ID notation previously used by Slivan et al. (2003, 2009) is retained, in which P_1 and P_2 denote prograde poles and P_3 and P_4 denote retrograde poles. The last two columns in the table give the estimated uncertainties for both poles' longitudes and latitudes respectively in degrees of arc.

The spin obliquity ε of each pole solution, calculated as the angle between the spin pole and the orbit pole, is given in Table 9. In the context of the spin poles, “prograde” and “retrograde” refer to poles whose obliquities are less than 90° and greater than 90° , respectively. “High obliquities” are near 90° and near the orbit plane; “low obliquities” are near either 0° (prograde) or 180° (retrograde) and near perpendicular to the orbit plane. Owing to the small orbital inclinations of the Koronis family, the obliquities of the two poles comprising each symmetric pair differ by less than 2° , well within the estimated uncertainties of the pole locations. In the last column the mean of each pair of obliquities is given as a single adopted mean obliquity for the object.

Table 10 summarizes very coarse estimates of axial ratios for the CI model shapes, noting that the model shapes for the two symmetric poles for each object are essentially identical except for being mirror-imaged. These axial ratios are very approximate, with uncertainties of at least ± 0.1 ; due to the limited number of data and observing geometries, the pole coordinates are considerably better constrained than are the derived shape models. In Table 10 for each object the first pair of model axial ratios given is based on spatial extents along Cartesian axes having the x - and z -directions aligned with the longest and polar axes, respectively. The second pair of axial ratios for each model is

Table 8
Spin vector results.

Asteroid	P_{sid} (h)	$\sigma(P_{\text{sid}})$ (h)	Pole ID	λ_0 ($^\circ$)	β_0 ($^\circ$)	Pole ID	λ_0 ($^\circ$)	β_0 ($^\circ$)	$\sigma(\lambda_0)$ ($^\circ$)	$\sigma(\beta_0)$ ($^\circ$)
(658) Asteria	21.02981	0.00003	P_3	124	-36	P_4	306	-39	5	5
(761) Brendelia	57.9949	0.0003	P_3	37	-47	P_4	212	-48	5	10
(811) Nauheima	4.000948	0.000002	P_1	150	+63	P_2	343	+60	5	5
(975) Perseverantia	7.223875	0.000005	P_3	67	-55	P_4	238	-58	5	10
(1029) La Plata	15.310657	0.000003	P_1	98	+60	P_2	281	+55	5	10
(1079) Mimosa	64.72834	0.00012	P_3	137	-37	P_4	318	-39	5	10
(1100) Arnica	14.53191	0.00002	P_1	123	+28	P_2	301	+28	5	10
(1245) Calvinia	4.8514754	0.0000005	P_3	54	-50	P_4	235	-43	5	5
(1336) Zeelandia	15.60188	0.00003	P_1	45	+5	P_2	226	+11	5	5
(1350) Rosselia	8.140103	0.000002	P_3	131	-84	P_4	269	-80	5	5
(1423) Jose	12.312679	0.000010	P_3	98	-80	P_4	237	-82	5	5
(1482) Sebastiana	10.489660	0.000003	P_3	93	-78	P_4	237	-79	5	5
(1618) Dawn	43.22002	0.00012	P_3	101	-57	P_4	268	-58	5	5
(1635) Bohrmann	5.864286	0.000003	P_3	9	-46	P_4	194	-46	5	10
(1725) CrAO	21.47246	0.00007	P_3	64	-39	P_4	241	-33	5	5
(1742) Schaifers	8.532708	0.000002	P_1	27	+71	P_2	195	+75	5	5
(1848) Delvaux	3.63911184	0.00000019	P_3	143	-83	P_4	348	-82	5	5
(2144) Marietta	5.4885454	0.0000012	P_1	145	+72	P_2	344	+70	5	5
(2209) Tianjin	9.452694	0.000003	P_1	19	+68	P_2	186	+72	5	5

based on fitted principal axes of moments of inertia, assuming uniform density inside the volume enclosed by the model shape (Drummond, 2014). The moments ratios agree with the spatial ratios to within 0.1, nominally corroborating the estimated uncertainty. The moments ratios also should be more physically meaningful than the spatial ratios, mindful that the moments remain subject to systematic effects if large-scale non-convex irregularities and/or craters are present on the asteroid, because such features will be filled in as flattened regions on the “photometric convex hull” model shape from convex inversion. In the final column θ_{MI} is the angular difference between the shortest principal axis calculated from the moments and the polar axis of the model shape. Caution is needed in interpreting deviations for models for which b/c is not large enough for the shape modeling to clearly distinguish the relative lengths of its b and c axes.

Renderings of the shape models themselves are presented in Fig. 5, mindful that details of the shape results from these relatively small lightcurve datasets are not very robust.

The spin vector directions of the four program objects (1350) Rosselia, (1423) Jose, (1482) Sebastiana, and (1848) Delvaux each lie within 15° of an ecliptic pole. As Koronis family members these objects share small orbit inclinations, thus their high-latitude spin vectors restrict Earth-based viewing aspects to be always close to equatorial. Because the lightcurves lack the information needed to properly scale the model shape in the direction along its polar axis, its b/c axial ratio outcome is sensitive to the shape of the initial ellipsoid. The reported value of the b/c ratio in each of these cases was identified based on the relative fit χ^2 values from among a series of trial inversion runs differing only by the b/c value supplied for the initial ellipsoid.

The spin vector analyses of the 19 program objects are each discussed individually in the following sections.

Table 9

Spin obliquities for the spin vectors given in Table 8.

Asteroid	Orbit pole ^a	Spin vector obliquities			Adopted ϵ	
(658) Asteria	(261°;+88°)	P_3	127°	P_4	128°	127°
(761) Brendelia	(294°;+88°)	P_3	138°	P_4	138°	138°
(811) Nauheima	(41°;+87°)	P_1	28°	P_2	28°	28°
(975) Perseverantia	(309°;+87°)	P_3	146°	P_4	147°	147°
(1029) La Plata	(300°;+88°)	P_1	32°	P_2	33°	32°
(1079) Mimosa	(240°;+89°)	P_3	127°	P_4	129°	128°
(1100) Arnica	(214°;+89°)	P_1	62°	P_2	62°	62°
(1245) Calvinia	(62°;+87°)	P_3	137°	P_4	136°	136°
(1336) Zeelandia	(7°;+87°)	P_1	83°	P_2	82°	82°
(1350) Rosselia	(50°;+87°)	P_3	172°	P_4	172°	172°
(1423) Jose	(329°;+87°)	P_3	171°	P_4	172°	171°
(1482) Sebastiana	(341°;+87°)	P_3	169°	P_4	169°	169°
(1618) Dawn	(13°;+87°)	P_3	147°	P_4	148°	148°
(1635) Bohrmann	(95°;+88°)	P_3	136°	P_4	136°	136°
(1725) CrAO	(29°;+87°)	P_3	127°	P_4	126°	126°
(1742) Schaifers	(62°;+88°)	P_1	17°	P_2	17°	17°
(1848) Delvaux	(242°;+89°)	P_3	173°	P_4	173°	173°
(2144) Marietta	(49°;+87°)	P_1	19°	P_2	19°	19°
(2209) Tianjin	(61°;+87°)	P_1	20°	P_2	19°	19°

^a The orbit pole is $(\Omega-90^\circ; 90^\circ - i)$ where the values of the osculating orbit elements used, longitude of ascending node Ω and inclination i , are ecliptic and equinox J2000.0 for epoch JD 2451800.5 (Shor, 1999).

Table 10

Model axial ratios for the spin vector results given in Table 8.

Asteroid	Spatial extents		Moments of inertia		
	a/b	b/c	a/b	b/c	θ_{MI}
(658) Asteria	1.5	1.0	1.5	1.0	6 ^{ob}
(761) Brendelia	1.3	1.3	1.3	1.4	2°
(811) Nauheima	1.1	1.5	1.0	1.6	2°
(975) Perseverantia	1.1	1.0	1.2	1.0	8 ^{ob}
(1029) La Plata	1.4	1.4	1.5	1.3	2°
(1079) Mimosa	1.1	1.2	1.2	1.2	9°
(1100) Arnica	1.2	1.0	1.2	1.0	15 ^{ob}
(1245) Calvinia	1.5	1.0	1.6	1.0	30 ^{ob}
(1336) Zeelandia	1.4	1.2	1.4	1.3	14°
(1350) Rosselia	1.5	1.2 ^a	1.5	1.2 ^a	12°
(1423) Jose	1.7	1.0 ^a	1.7	1.1 ^a	55 ^{ob}
(1482) Sebastiana	1.6	1.1 ^a	1.6	1.1 ^a	6 ^{ob}
(1618) Dawn	1.6	1.0	1.6	1.0	45 ^{ob}
(1635) Bohrmann	1.4	1.3	1.3	1.3	17°
(1725) CrAO	1.2	1.3	1.2	1.4	2°
(1742) Schaifers	2.1	1.1	2.0	1.1	23 ^{ob}
(1848) Delvaux	1.7	1.4 ^a	1.7	1.4 ^a	2°
(2144) Marietta	1.4	1.0	1.3	1.0	36 ^{ob}
(2209) Tianjin	1.3	1.3	1.3	1.2	3°

^a b/c is less reliably determined for this object that has a high-latitude spin axis.

^b Caution is needed in interpreting the deviation θ_{MI} for this model that has $b/c \lesssim 1.1$.

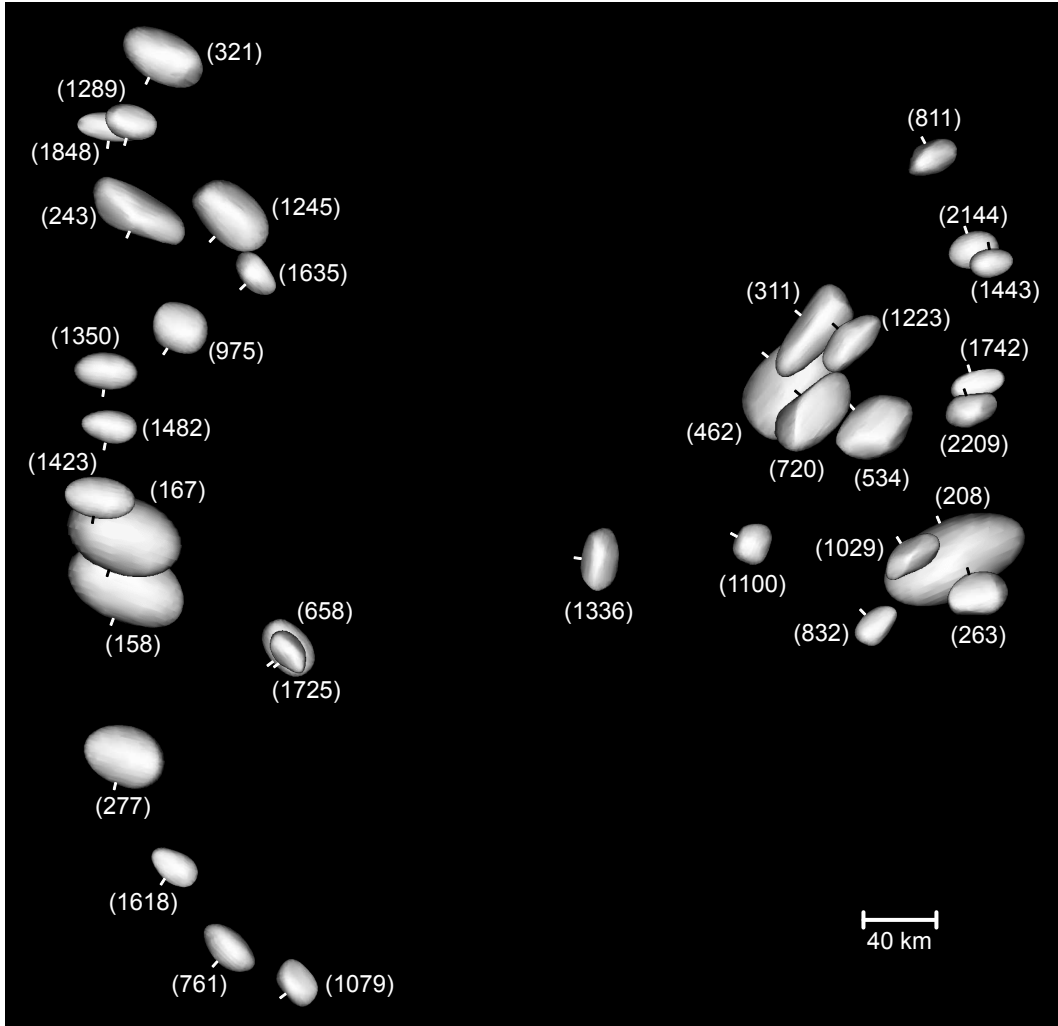


Figure 5: Shape model renderings of the 34 objects comprising the Koronis family spin vector sample, scaled to represent approximate sizes. The overall linear scale is set by the long dimension of (243) Ida (Belton et al., 1996), and each rendering's relative size is calculated using its model axial ratios so that the ellipsoidal cross-sectional area of the broadside equatorial view is proportional to the flux ratio corresponding to its catalog H magnitude difference from Ida. Views are equatorial and broadside to the longest axis, fully illuminated using an artificial scattering law to reveal shape features. A tick mark on each rendering indicates the object's north pole, with its position angle equal to the spin obliquity. The objects are arranged as in the graph shown in Fig. 29 so that rotation frequency increases toward the top and spin obliquity increases numerically toward the left.

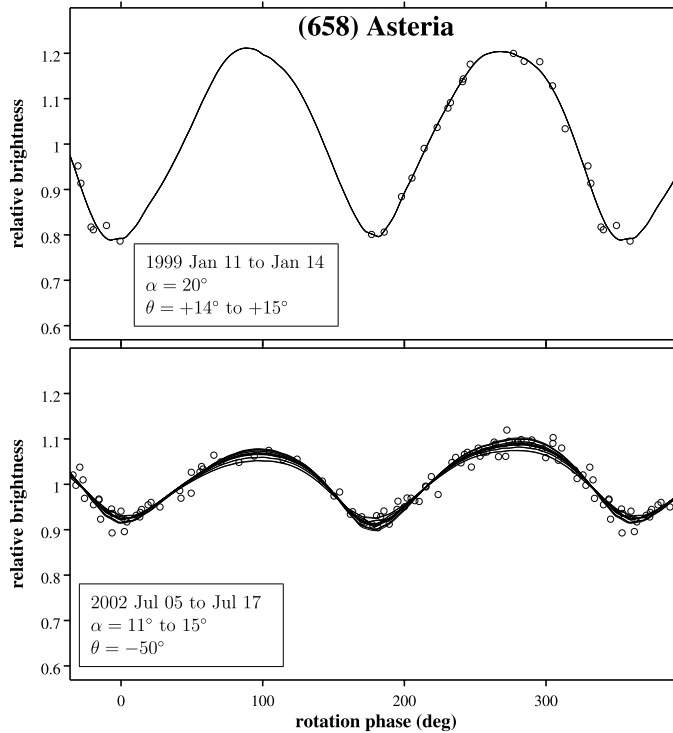


Figure 6: Selected lightcurve fits for (658) Asteria with a pole P_4 at $(306^\circ; -39^\circ)$, plotted as brightness vs. sidereal rotation phase in degrees. Data are shown as open circles, and solid curves represent model brightnesses. Changes in the underlying lightcurve shape during the course of the observations appear as non-overlapping model curves. The legends give the UT dates of the observations and the corresponding ranges of solar phase angles α and sub-PAB latitudes θ ; the graphs are presented in order of decreasing θ . The RMS error of the fit to the combined data set of lightcurves corresponds to 0.012 mag.

3.2. (658) Asteria

The Asteria lightcurve data set includes six apparitions spanning 24 years, with a 150-degree gap in aspect ecliptic longitude coverage centered near 245° . Non-overlapping segments of relative photometry from 1999 (Slivan et al., 2008) do not permit confidently determining an epoch for the initial analysis for the sidereal period, even though the lightcurves combined record about half of a rotation. Epoch information available from the other five apparitions nevertheless constrains the sidereal rotation count to three possibilities, from which SPA identifies the correct period and retrograde spin. The maximum epoch interval corresponds to 9967 sidereal rotations.

Using the lightcurves from all six apparitions, CI finds a pair of pole solution regions having the expected symmetry. Selected lightcurve fits are presented in Fig. 6.

3.3. (761) Brendelia

The lightcurves of Brendelia from the 2001 apparition (Slivan et al., 2008) are too incomplete for Fourier series fitting and were not included in the analysis of epochs for the sidereal rotation period. Epochs from 2003–2013 determine an unambiguous sidereal rotation count, from which SPA identifies retrograde rotation. The maximum epoch interval corresponds to 1540 sidereal rotations.

Brendelia's 58-h rotation period precludes analyzing the uncombined lightcurves as relative photometry; instead, the standard-calibrated R data were transformed to the same brightness zero-point as the V data using color information from Table 5 and analyzed together as standard-calibrated photometry. Analyzing the calibrated lightcurves clearly locates the pole regions, and selected lightcurve fits are presented in Fig. 7. Our sidereal period for Brendelia agrees with that of Āurech et al. (2018), and our P_4 is 5 degrees of arc from their single pole solution.

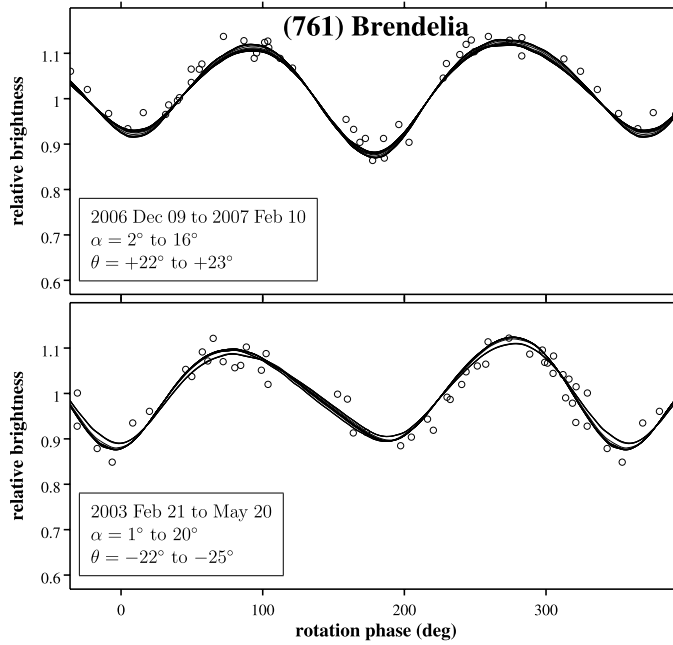


Figure 7: The same as Fig. 6 but for (761) Brendelia with a pole P_4 at $(212^\circ; -48^\circ)$. The RMS error of the fit corresponds to 0.026 mag.

3.4. (811) Nauheima

Lightcurves of Nauheima are available from seven apparitions spanning 23 years with good coverage in PAB longitude. The asymmetric shapes and consistently rather low amplitude of the lightcurves make it harder to accurately locate features that are related to low-order asteroid shape. Intervals between the filtered epochs determine an unambiguous sidereal rotation count, for which SPA favors the prograde period solution; the maximum epoch interval corresponds to 49129 sidereal rotations.

The RMS error of the SPA fit to the epochs is larger than is typical for the corresponding analysis for the other sample objects, and is dominated by the residual for the epoch estimated from the incomplete lightcurve from 1989. Before proceeding with CI the rotation counting was checked by directly comparing similarly-shaped lightcurves to determine intervals, an approach that is insensitive to systematic errors that may be present in the identifications of individual epochs. The lightcurves from the apparitions of 2004 and 2005 have similar shapes, constraining the sidereal period to two candidate ranges within the synodic constraint of 4.0006 to 4.0016 h. The interval elapsed between the reflex aspect pair of 2004 and 2007 rules out one of the ranges and reduces the span of the other, which is then further narrowed first by the similar-aspect pair of 1988 and 1998, and then finally by the maximum interval of 1984 and 2007 to corroborate the sidereal rotation counts determined from the Fourier-filtered epochs.

The observed viewing aspects of Nauheima are clustered near four ecliptic longitudes, and weighting the Nauheima lightcurve data on the basis of epochs for CI input produces a very lopsided distribution in aspect coverage; to aid the CI analyses for this object, the weighting was determined based on viewing aspects. CI finds the pole regions at ecliptic longitudes about 50° different from those found by SPA; the CI locations are favored here because they incorporate lightcurve amplitude information about pole longitude that is unavailable to SPA. The pole-on view of the shape model has a triangular profile, and selected lightcurve fits are presented in Fig. 8.

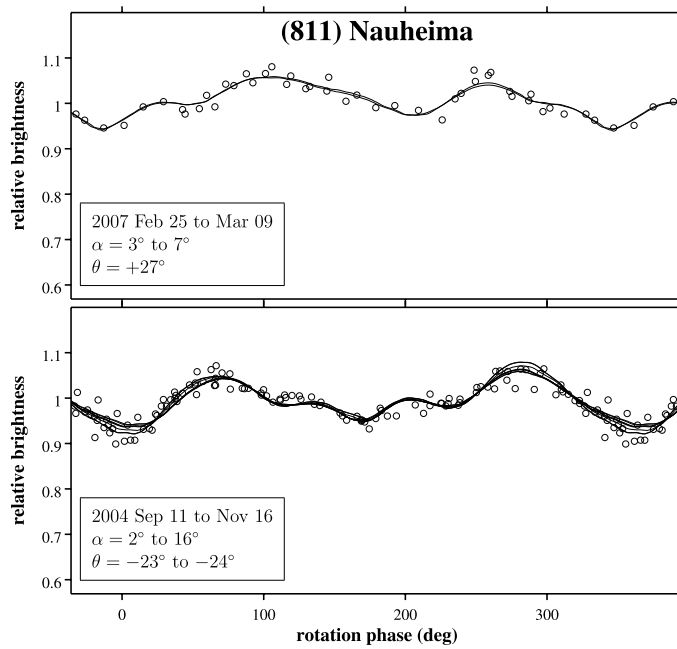


Figure 8: The same as Fig. 6 but for (811) Nauheima with a pole P_2 at $(343^\circ; +60^\circ)$. The RMS error of the fit corresponds to 0.018 mag.

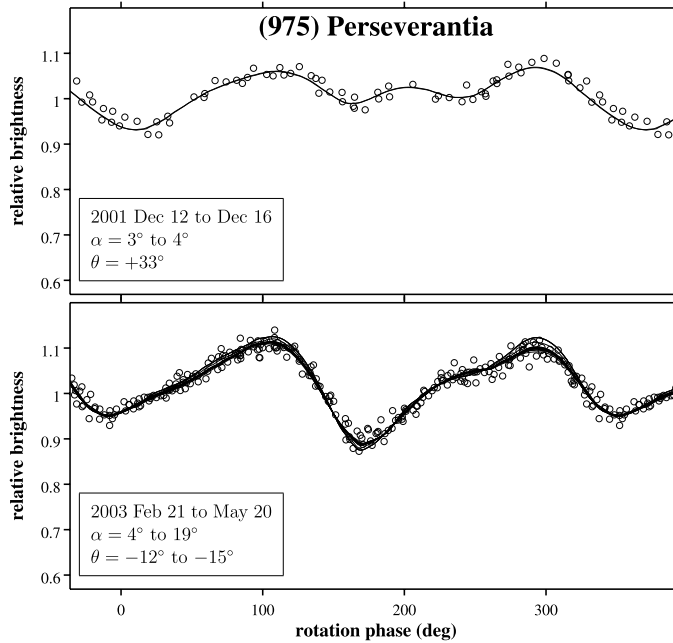


Figure 9: The same as Fig. 6 but for (975) Perseverantia with a pole P_4 at $(238^\circ; -58^\circ)$. The RMS error of the fit corresponds to 0.014 mag.

3.5. (975) Perseverantia

The combined data set of Perseverantia lightcurves reported in this work together with those summarized by Slivan et al. (2008) spans more than 11 years. *J*-band observations by Veeder et al. (1995) made on two nights during one more apparition in 1990 yield a folded composite lightcurve covering about a quarter of a rotation, just enough to locate an additional epoch that nearly doubles the span of observations to almost 23 years.

SPA analysis of the epochs constrains the sidereal period to a single pair of candidate solutions with corresponding pole regions, favoring the retrograde solution over the prograde. CI confirms that the retrograde poles are correct, indicating two oval regions exhibiting the expected symmetry. The maximum epoch interval corresponds to 27516 sidereal rotations. Selected lightcurve fits presented in Fig. 9.

Our sidereal period for Perseverantia agrees with a model reported by Ďurech et al. (2019), but our pair of pole solutions is about 12° farther north in latitude than is their pair.

3.6. (1029) La Plata

Lightcurves of La Plata span over 31 years, starting with the 1975 photographic lightcurve from Lagerkvist (1978). The epochs analyses constrain the sidereal period to a single prograde solution, for which CI locates oval pole regions having the expected symmetry. The maximum epoch interval corresponds to 18007 sidereal rotations, and selected lightcurve fits are presented in Fig. 10.

Our results for La Plata do not agree with those reported by Ďurech and Hanuš (2018)—our sidereal period is significantly longer, and while specific error estimates for their pole do not seem to have been reported, our pole locations P_1 and P_2 differ from theirs by 12 and 33 degrees of arc, respectively. It is instructive to note that their period value is close to an alias period in our analysis, and their pair of pole solutions is not symmetric with respect to the PGC pole; instead its 28 degrees of arc departure from symmetry indicates that at least one of its pole locations is not correct. Ďurech et al. (2019) revisited the modeling of La Plata and reported a single pole that is 7° from our P_2 , and a sidereal period that is plausibly consistent within its order of magnitude error estimate.

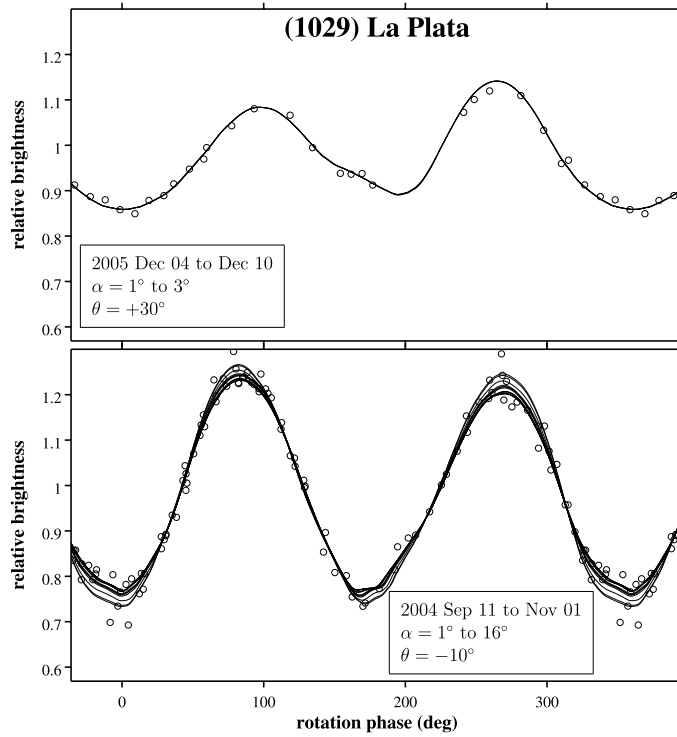


Figure 10: The same as Fig. 6 but for (1029) La Plata with a pole P_2 at $(281^\circ; +55^\circ)$. The RMS error of the fit corresponds to 0.021 mag.

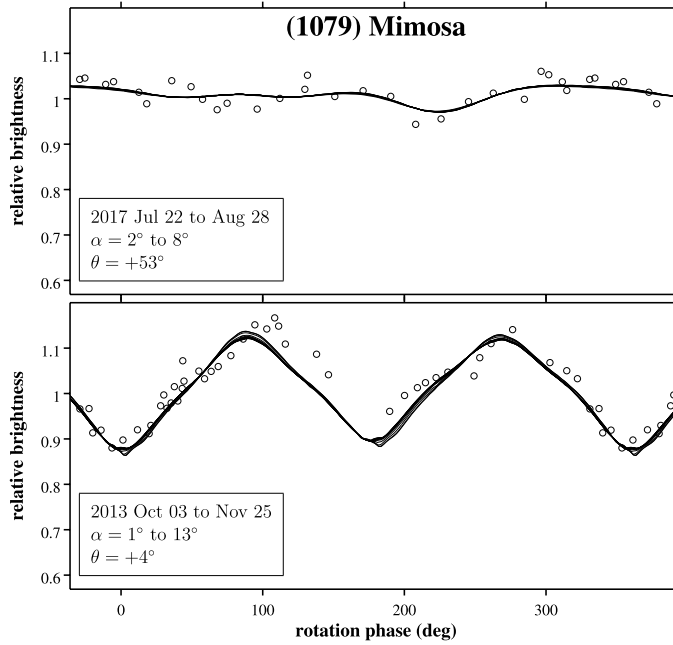


Figure 11: The same as Fig. 6 but for (1079) Mimosa with a pole P_3 at $(137^\circ; -37^\circ)$. The RMS error of the fit corresponds to 0.033 mag.

3.7. (1079) Mimosa

The Mimosa lightcurve data set includes eight apparitions spanning nearly 38 years. Epoch information estimated from the incomplete 2003 lightcurve was assigned a larger uncertainty; low-amplitude lightcurves recorded in 1983 (Binzel, 1987) and in 2017 lack features clearly related to low-order shape and were not included in epochs analysis. Epochs from the six apparitions included in the initial analysis constrain the sidereal rotation count to two possibilities, one prograde and one retrograde, differing by half a rotation over the observed interval. SPA locates a pair of symmetric pole regions for each candidate rotation count, favoring the retrograde solutions.

Mimosa's 65-h rotation period precludes analyzing the uncombined lightcurves as relative photometry; instead, the standard-calibrated B , V , and r' data were transformed to the same brightness zero-point as the R data and analyzed together as standard-calibrated photometry using $B-V = 0.81 \pm 0.02$ (Binzel, 1987), $V-R = 0.477 \pm 0.014$ (Slivan et al., 2008), and $r'-R$ from Table 5. Using the lightcurves from all eight apparitions, CI locates the two pairs of candidate pole regions corresponding to SPA, plus two rejected spurious pairs closer to the ecliptic which would require nonphysical model shapes having $b/c < 1$. CI by itself does not resolve the direction of spin from among the remaining candidate poles, likely as a consequence of having only limited information available at viewing geometries away from the higher-amplitude aspects. Nevertheless, the strong correspondence of the CI retrograde regions locations with the SPA regions, and the poorer correspondence of the prograde regions, corroborate the SPA preference for retrograde rotation. The maximum epoch interval corresponds to 4967 sidereal rotations, and selected lightcurve fits are presented in Fig. 11.

Our sidereal period for Mimosa is significantly shorter than a result reported by Āurech et al. (2020); their value is close to an alias period in our analysis. Our pole solutions agree with theirs in latitude, but are smaller in longitude by 7 to 8 degrees of arc which is between 2 and 3 times their estimated errors.

3.8. (1100) Arnica

Lightcurve data recorded during the nine observed apparitions of Arnica are clustered near four different viewing aspects. While the lightcurves from aspect ecliptic longitudes near 25° are doubly-periodic and relatively symmetric with amplitudes larger than 0.2 mag., near 185° the lightcurves are asymmetric with a distorted fainter maximum. At the aspects near 105° and 280° the lightcurve is singly periodic with amplitude not exceeding 0.15 mag.

Reliable identification of lightcurve features for epochs determination is limited to the larger-amplitude apparitions. The epochs analysis includes unpublished lightcurves recorded during the 2005 apparition (data provided by R. Roy and

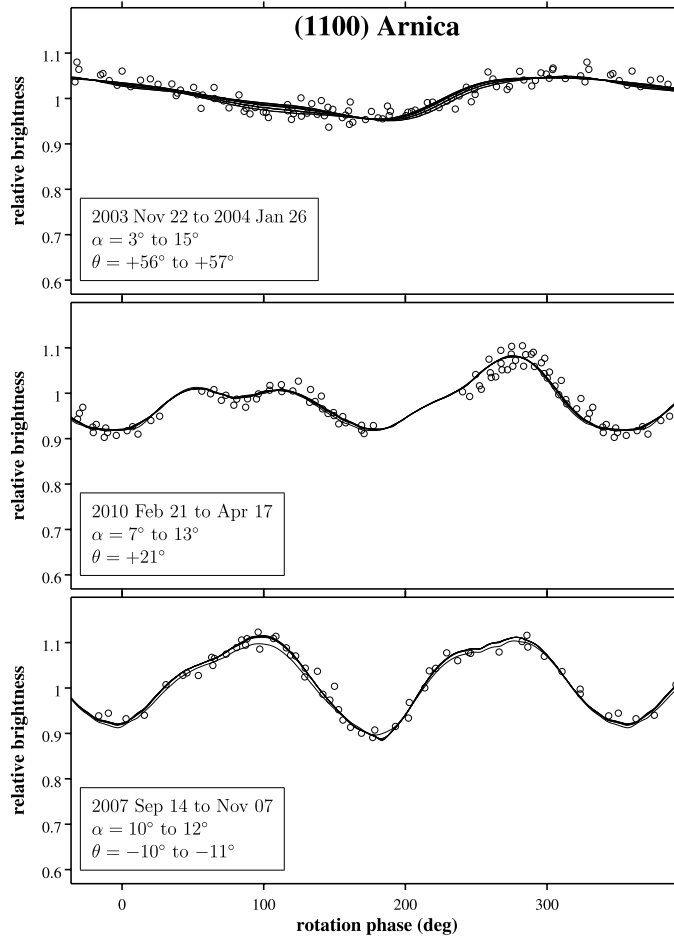


Figure 12: The same as Fig. 6 but for (1100) Arnica with a pole P_2 at $(301^\circ; +28^\circ)$. The RMS error of the fit corresponds to 0.016 mag.

R. Behrend) to establish a longer maximum time interval between well-defined epochs. Although applying the Fourier filtering approach to the singly-periodic lightcurves does yield credible epochs, they cannot simply be combined in a single analysis with the epochs from the doubly-periodic aspects, because epochs from lightcurves having such significantly different shapes are unlikely to satisfy the assumption that every epoch in the analysis corresponds to either the same astero-centric longitude or its reflex. Instead, the two subsets are analyzed separately. Epochs from the doubly-periodic lightcurves observed in 2005, 2007, 2010, and 2012 constrain the sidereal period to a single pair of possible values, one each prograde and retrograde. The epochs from the singly-periodic lightcurves observed in 2004, 2009, and 2014 require integer numbers of rotations between them, which likewise constrains period candidates to a single pair prograde and retrograde. Only the prograde candidate period is consistent with both subsets.

CI locates the pair of well-defined pole location regions with the expected symmetry. To estimate the error in the sidereal period from the combined analysis of all apparitions, the RMS error of the SPA fit to the larger-amplitude epochs that span 7.6 years is scaled by the ratio 7.6/15 to account for the larger number of sidereal rotations that occur over the entire 15-year span of lightcurve data. The interval between the first and last dates of observations corresponds to 9079 sidereal rotations, and selected lightcurve fits are presented in Fig. 12.

3.9. (1245) *Calvinia*

Before beginning analyses of the *Calvinia* data, the inconsistency of the epochs among the lightcurves from 1977 that was identified by Slivan et al. (2008) was investigated. The explanation is that the photoelectric data of *Calvinia* from 1977 August that were archived into the Asteroid Photometric Catalogue (Lagerkvist et al., 1987) were incorrectly

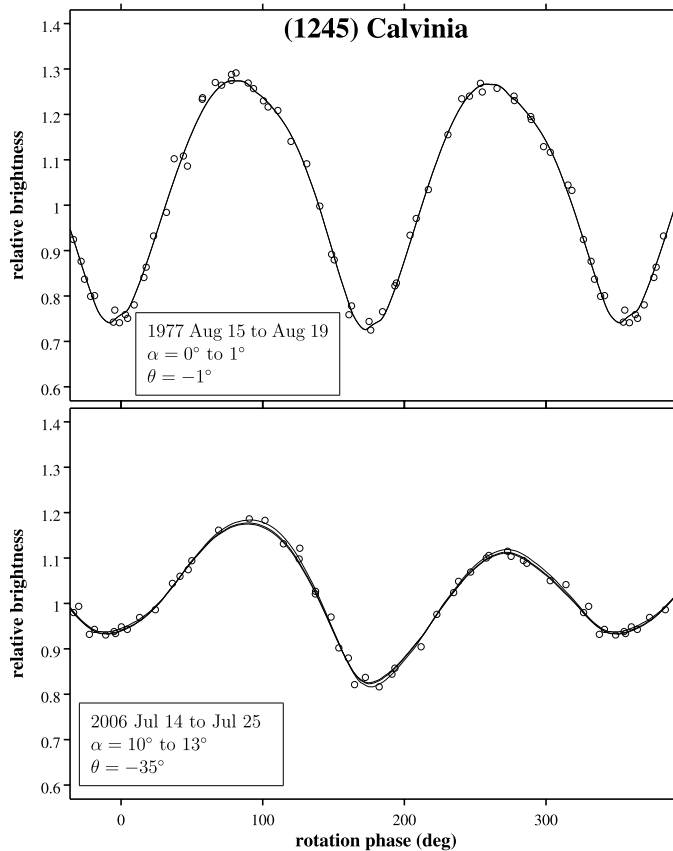


Figure 13: The same as Fig. 6 but for (1245) Calvinia with a pole P_4 at $(235^\circ; -43^\circ)$. The RMS error of the fit corresponds to 0.012 mag.

identified there as not being light time corrected, when in fact the original data (Tedesco, 1979; Degewij et al., 1979) had already been light time corrected when first published (E. Tedesco, personal communication). This error has propagated into the current version of the APC (Lagerkvist and Magnusson, 2011), in which the time tags themselves for this lightcurve are now systematically incorrect because there the light time correction has been applied twice.

The filtered epochs from 2002 through 2012 yield a single possible count of sidereal rotations, from which SPA is able to reject the prograde solution leaving an unambiguous retrograde sidereal period. Including the data from 1977 further refines the period so that the maximum epoch interval corresponds to 63791 sidereal rotations.

CI identifies well-defined pole regions that agree with SPA and exhibit the expected symmetry. Selected lightcurve fits are presented in Fig. 13. The model predicts a lightcurve for the 1975 photographic observations that appears consistent “by eye” with the data, but those observations were excluded from the analysis because including them distorts the shape fitting and yields a model that is inconsistent with the low-noise photoelectric data from 1977. Our poles and sidereal period for Calvinia are consistent with the results reported by Āurech et al. (2016).

3.10. (1336) Zeelandia

The observed viewing aspects of Zeelandia are broadly clustered near four ecliptic longitudes, whose lightcurves exhibit markedly different shapes and amplitudes. In particular, the lightcurves observed in 2010 are singly-periodic with low amplitude, and those from its reflex aspect apparitions in 2007 and 2013 are doubly-periodic but very asymmetric. Even though those three apparitions initially were excluded from the analysis of epochs to count sidereal rotations, epochs from the remaining six apparitions still included were sufficient to unambiguously determine the rotation count. Within the constraint of that count result, the epochs measured from the asymmetric lightcurves were confirmed to be consistent with predictions based on the epochs from the symmetric lightcurves and added to the

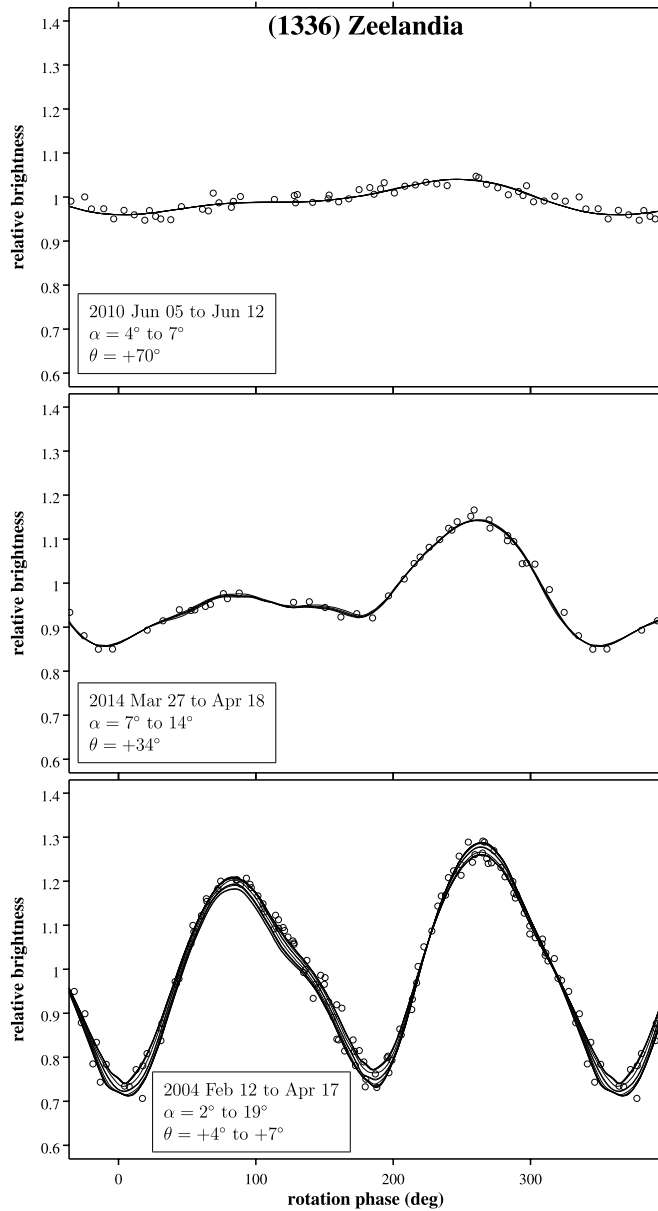


Figure 14: The same as Fig. 6 but for (1336) Zeelandia with a pole P_1 at $(45^\circ; +5^\circ)$. The RMS error of the fit corresponds to 0.016 mag.

epochs analyses for SPA, which indicated pole regions close to the ecliptic and was able to distinguish the prograde direction of spin. The maximum epoch interval corresponds to 8545 sidereal rotations.

Using CI the two pole regions are very well-defined. Selected lightcurve fits are presented in Fig. 14. At near-equatorial aspects the two lightcurve maxima are comparable in brightness (bottom graph), but at mid-latitude aspects the maxima are asymmetric, with one much fainter than the other as it approaches the level of the minima (center graph). As is discussed in Sec. 3.15 for (1635) Bohrmann, this behavior corresponds to the presence of a relatively large-scale planar region spanning astero-centric mid-latitudes on the convex model shape. The 14° deviation of the Zeelandia model's principal axis from its polar axis suggests that the region could represent a large concave feature on the asteroid, such as a crater.

Our sidereal period agrees with that reported by Āurech et al. (2019), however our pole latitudes are 11° farther south and closer to the ecliptic plane.

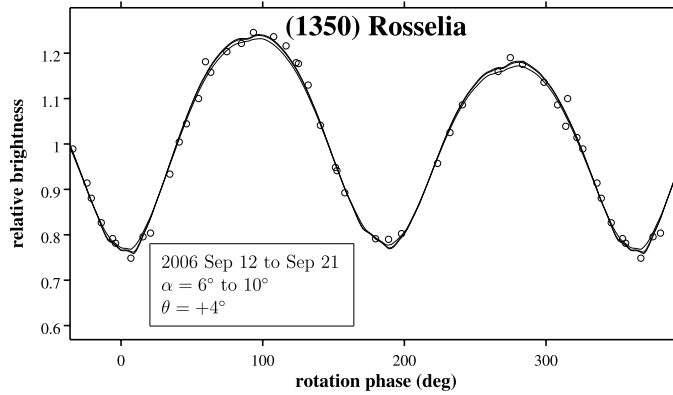


Figure 15: The same as Fig. 6 but for (1350) Rosselia with a pole P_3 at $(131^\circ; -84^\circ)$. Only a single graph is selected because the viewing aspect always is close to equatorial. The RMS error of the fit corresponds to 0.023 mag.

3.11. (1350) Rosselia

Lightcurves of Rosselia span nearly 33 years, starting with the 1975 photographic lightcurve from Lagerkvist (1978). The 1991 lightcurve from Veeder et al. (1995) is too incomplete to locate extrema and was excluded from the initial sidereal period determination. The remaining epochs from 1975 through 2007 identify three candidate sidereal rotation counts, from which SPA establishes the correct retrograde solution with pole regions at high south latitudes and a maximum epoch interval corresponding to 35280 sidereal rotations.

The CI pole regions satisfy the expected symmetry with respect to the PGC pole, but their longitudes are only weakly distinguished. The scant six points comprising the 1991 composite lightcurve were retained only to confirm consistency of the CI model and do not affect the results. Because the pole is at a high latitude, the model shape b/c axial ratio remains poorly determined as described in Sec. 3.1. Selected lightcurve fits are presented in Fig. 15.

Pole solutions for Rosselia that have been reported by Hanuš et al. (2013) and Āurech et al. (2016) do not agree with each other, and our derived pair of spin poles are about ten to twenty degrees farther south in ecliptic latitude and differ in longitude from all of them. Our sidereal period agrees with Hanuš et al. (2013), and our P_3 is 13 degrees of arc from their single pole solution. Āurech et al. (2016) report a sidereal period which is only slightly shorter, and pole solutions which are 24 degrees and 23 degrees from our P_3 and P_4 , respectively.

3.12. (1423) Jose

Lightcurves of Jose are available from five consecutive apparitions, comprising the only object data set in the analysis sample having data from fewer than six apparitions. The epochs are nevertheless sufficient to unambiguously count sidereal rotations, and for SPA to identify retrograde spin. The maximum epoch interval corresponds to 3610 sidereal rotations. The spin vector solution regions are strongly constrained in latitude near the south ecliptic pole; the longitudes are less strongly distinguished but do satisfy the expected symmetry. The model shape b/c axial ratio remains poorly determined given the high latitude of the pole, as described in Sec. 3.1. Selected lightcurve fits are presented in Fig. 16. Hanuš et al. (2013) studied Jose; our sidereal period agrees with theirs and our P_3 is 4 degrees of arc from their single reported pole solution.

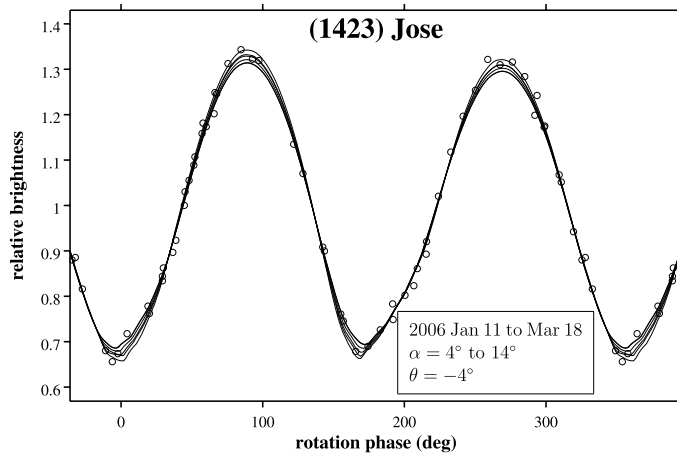


Figure 16: The same as Fig. 6 but for (1423) Jose with a pole P_3 at $(98^\circ; -80^\circ)$. Only a single graph is selected because the viewing aspect always is close to equatorial. The RMS error of the fit corresponds to 0.024 mag.

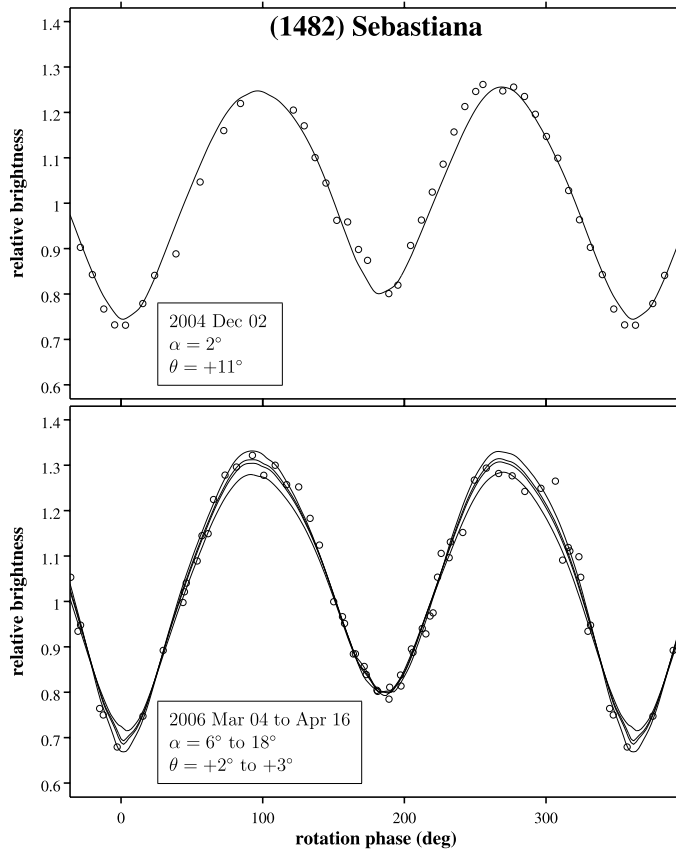


Figure 17: The same as Fig. 6 but for (1482) Sebastiana with a pole P_4 at $(237^\circ; -79^\circ)$. The RMS error of the fit corresponds to 0.024 mag.

3.13. (1482) Sebastiana

Epochs analysis for Sebastiana determines an unambiguous sidereal rotation count, whose retrograde solution is favored by SPA. The maximum epoch interval corresponds to 18890 sidereal rotations. Sebastiana was the only program object for which the CI convexity regularization weight parameter needed to be changed from its default value. Although the shapes of the pole solution regions are somewhat weakly defined, the poles are unambiguously near the south ecliptic pole, leaving the model shape b/c axial ratio poorly determined as described in Sec. 3.1. Selected lightcurve fits are presented in Fig. 17.

Our sidereal period agrees with the result of Hanuš et al. (2011) within its reported precision. Our P_3 and P_4 are 11 and 13 degrees of arc respectively from their corresponding poles, differences which are comparable to their own estimated errors.

3.14. (1618) Dawn

The Dawn lightcurve data set includes six apparitions spanning nearly 18 years. Lightcurves from the 2020 apparition are too incomplete for Fourier series fitting and were not included in the analysis of epochs for the sidereal rotation period. Epochs from the remaining five apparitions determine an unambiguous sidereal rotation count, from which SPA favors retrograde rotation. The maximum epoch interval corresponds to 3559 sidereal rotations.

Dawn's 43-h rotation period precludes analyzing the uncombined lightcurves as relative photometry; instead, the standard-calibrated V data were transformed to the same brightness zero-point as the R data using $V-R = 0.436 \pm 0.014$ (Slivan et al., 2008) and analyzed together as standard-calibrated photometry. The data from the apparitions in 2017, 2020, and 2021 that had not been put onto a standard system were prepared for analysis as composite lightcurves of relative photometry.

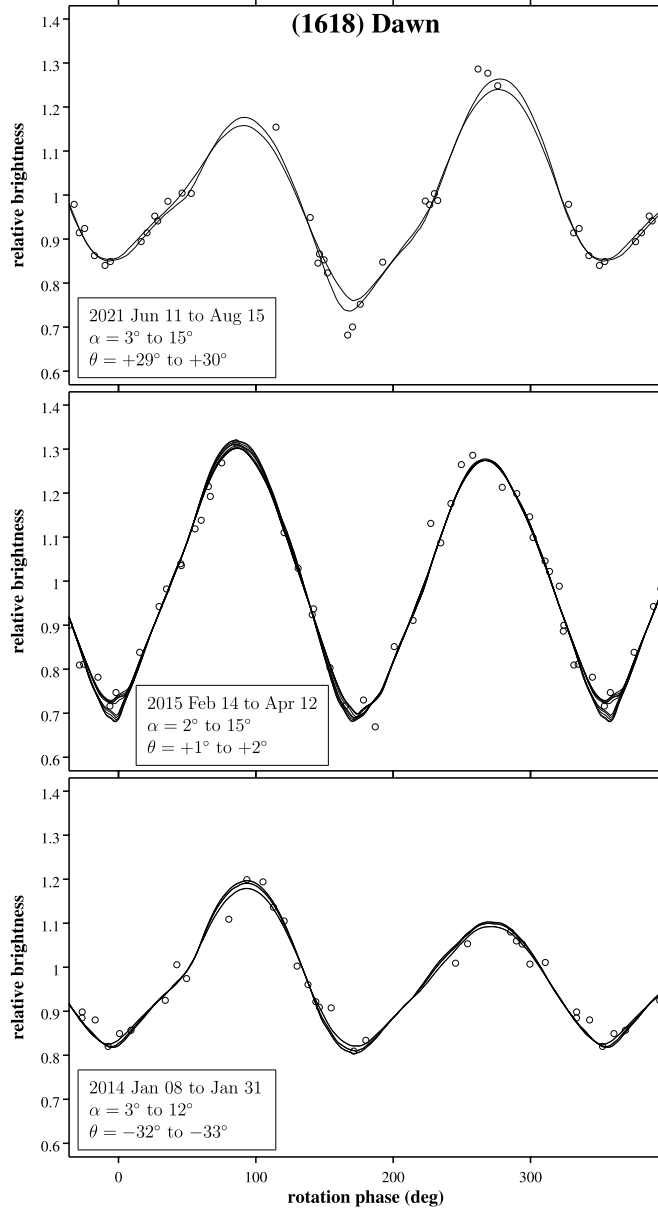


Figure 18: The same as Fig. 6 but for (1618) Dawn with a pole P_3 at $(101^\circ; -57^\circ)$. The RMS error of the fit corresponds to 0.027 mag.

CI agrees with SPA to favor retrograde rotation, and locates a pair of retrograde pole solution regions which exhibit the expected symmetry. Selected lightcurve fits are presented in Fig. 18. Our sidereal period for Dawn is consistent with that reported by Hanuš et al. (2013) within its error, and our pair of pole solutions are about 30 degrees of arc from theirs which is consistent with their reported uncertainties of 10 to 20 degrees.

3.15. (1635) Bohrmann

The lightcurves of Bohrmann exhibit markedly different shapes depending on viewing aspect. During the similar-aspect apparitions in 2003 and 2008, and at approximately the reflex observing direction in 2011, the lightcurves were singly periodic with one relatively undistorted maximum comprising half of the rotation phase, and the other half nearly flat at the minimum brightness. To use Fourier series model fits to identify epochs from these lightcurves despite their

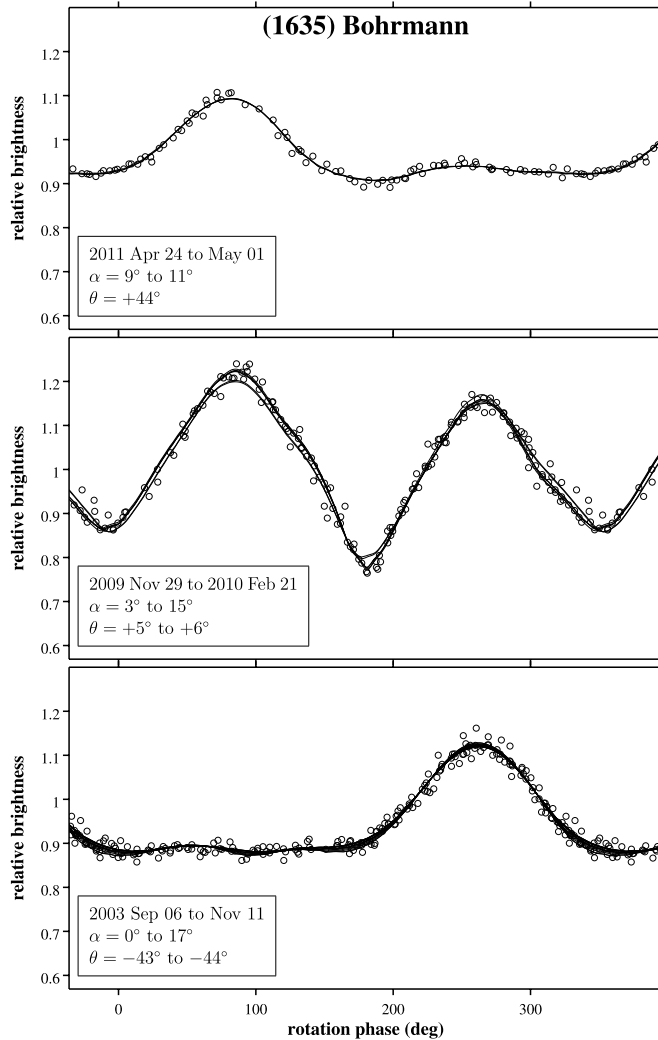


Figure 19: The same as Fig. 6 but for (1635) Bohrmann with a pole P_3 at $(9^\circ; -46^\circ)$. The RMS error of the fit corresponds to 0.018 mag.

almost entirely “missing” one of the maxima, only the half of rotation phase centered on the undistorted maximum was retained and fit at half the rotation period.

The available epoch data unambiguously count sidereal rotations, and SPA identifies retrograde spin. The maximum epoch interval corresponds to 13219 sidereal rotations. CI locates well-defined pole regions that are consistent with those from SPA. Selected lightcurve fits are presented in Fig. 19, which shows that opposite lightcurve maxima were distorted in 2003 and 2011. The model shapes show a large-scale planar feature, and the 17-degree difference between the model’s shortest principal axis and its polar axis is the largest deviation among those models for which $b/c > 1.1$, suggesting that a concave region on the asteroid, such as a large crater corresponding to the planar feature on the model, is responsible for the distorted lightcurve maxima as shown in Fig. 20.

Our sidereal period and poles for Bohrmann agree with the published results of Hanuš et al. (2011). Our P_3 and P_4 are respectively 9 and 12 degrees of arc from their poles, which carry their own estimated errors of about 10 degrees of arc.

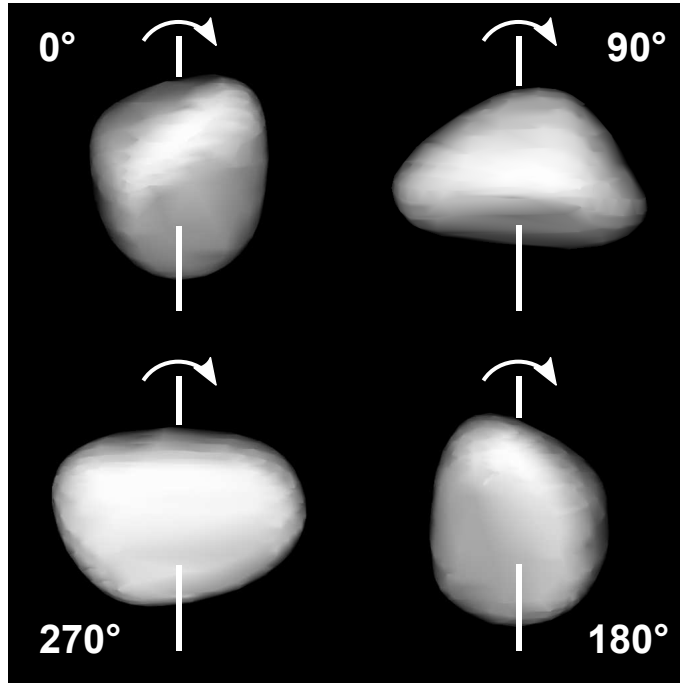


Figure 20: Shape model for the P_3 solution of (1635) Bohrmann showing its axis and direction of spin, rendered for a sub-observer latitude of -43° to correspond to the lightcurves in the bottom graph in Fig. 19. At rotation phase 270° the planar region is about 25 degrees from face-on and does not reduce the projected area of the model for the undistorted lightcurve maximum, but at what would be the opposite maximum at 90° the region is foreshortened at about 65 degrees from face-on, reducing the overall projected area for a lightcurve brightness that is not much different from the nominal minima at 0° and 180° .

3.16. (1725) CrAO

Lightcurves of CrAO are available from seven apparitions spanning 17 years. The larger-amplitude lightcurves are asymmetric in time with distorted maxima, requiring extra care to locate the extrema for epochs analyses. The smaller-amplitude lightcurve from the 2018 apparition is too incomplete to confidently locate extrema, and was excluded from epochs analysis. Epochs measured from the other six apparitions are sufficient to determine the sidereal period and identify retrograde spin; the maximum interval corresponds to 6676 sidereal rotations.

To include the data from 2018 in the CI analyses, its short non-overlapping individual lightcurves were combined into a single lightcurve of relative photometry by referencing all five nights' measurements to the same comparison star, and then compositing them in time and in brightness. Using the lightcurves from all seven apparitions, CI locates pole regions that are consistent with those from SPA. Selected lightcurve fits are presented in Fig. 21.

3.17. (1742) Schaifers

Prior to comprehensive analysis of the Schaifers data set, folding the rather sparsely-sampled lightcurves from 1983 (Binzel, 1987) at the improved synodic rotation period (Slivan et al., 2008) raised doubt about the reality of the unusually large amplitude of the original published composite lightcurve. Its asymmetric very deep minimum was recorded only on one night, whose lightcurve brightness zero-point relative to the composite was based on a single data point that overlaps other rotation phase coverage. Folding at the improved period revealed phase overlap of a second measurement, but its brightness zero-point to match the composite is more than 0.3 mag. different from that of the first point, indicating that at least one of the two brightness measurements is incorrect. Shifting the Oct. 9 lightcurve in brightness to agree at the second phase overlap instead of the first yields a composite lightcurve with overall shape and smaller amplitude both comparable to those observed for Schaifers during the other apparitions, thus we conclude that the brightness of the first overlapping point likely is incorrect, and that the lightcurve amplitude at the 1983 observing aspect was not so extreme. We note also that there are corroborating hints of possible systematic errors in the standard

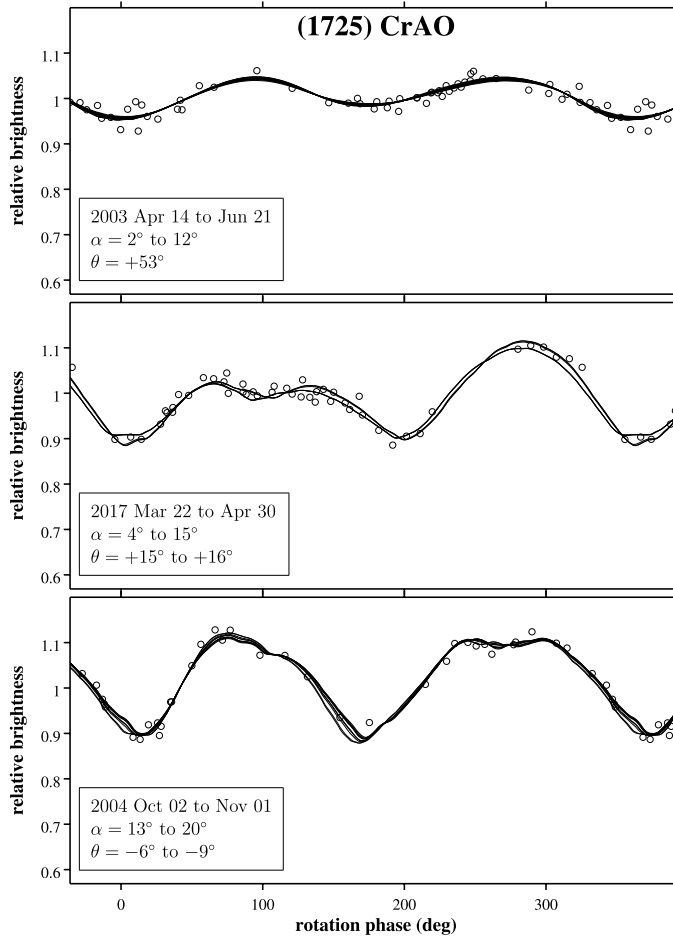


Figure 21: The same as Fig. 6 but for (1725) CrAO with a pole P_3 at $(64^\circ; -39^\circ)$. The RMS error of the fit corresponds to 0.013 mag.

calibrations of lightcurves of other objects that were recorded during the same observing run with Schaifers in 1983 (Slivan et al., 2009).

The full set of Schaifers epochs constrains the sidereal period to a single pair of candidate solutions, favoring the prograde solution over the retrograde. CI indicates two roughly oval regions which exhibit the expected symmetry. The maximum epoch interval corresponds to 33454 sidereal rotations. Selected lightcurve fits are presented in Fig. 22.

Our sidereal period for Schaifers agrees with the results of Hanuš et al. (2011) and Hanuš et al. (2013) to within their published precisions, but our poles differ considerably from theirs by 17 to 23 degrees of arc overall, individually different in longitude, in latitude, or in both. Neither of their pole pairs are consistent with the expected symmetry with respect to the PGC pole; instead they depart significantly by 11 to 14 degrees of arc which suggests that some systematic problem likely is present.

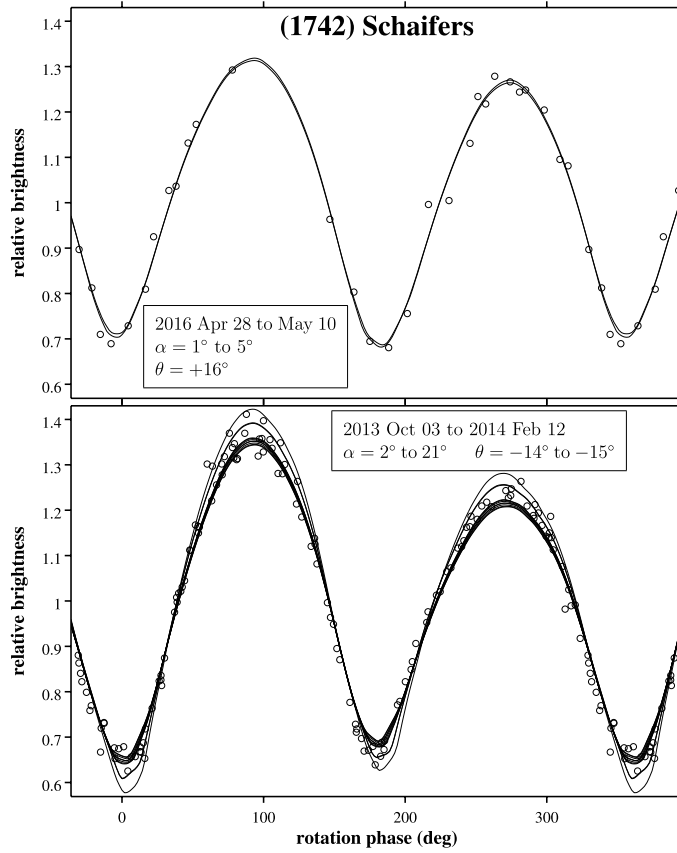


Figure 22: The same as Fig. 6 but for (1742) Schaifers with a pole P_1 at $(27^\circ; +71^\circ)$. The RMS error of the fit corresponds to 0.030 mag.

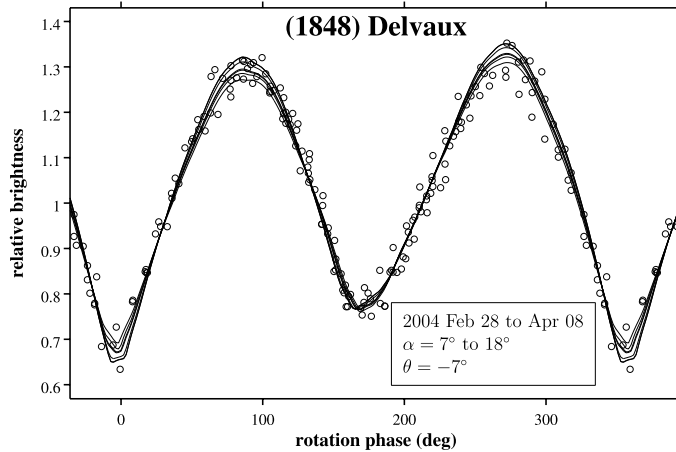


Figure 23: The same as Fig. 6 but for (1848) Delvaux with a pole P_3 at $(143^\circ; -83^\circ)$. Only a single graph is selected because the viewing aspect always is close to equatorial. The RMS error of the fit corresponds to 0.031 mag.

3.18. (1848) Delvaux

For spin vector and shape analysis of Delvaux an unpublished lightcurve recorded during the 2011 apparition (data provided by R. Roy and R. Behrend) was also included. The lightcurve amplitude during each of the seven observed apparitions was greater than 0.5 mag, suggesting a high-latitude spin vector and relatively elongated shape. Epochs analyses yield an unambiguous sidereal period and retrograde spin, for which the maximum epoch interval corresponds to 27271 sidereal rotations.

The spin vector is strongly constrained to be near the south ecliptic pole, thus the solution region ecliptic longitudes are only weakly indicated, and the model shape b/c axial ratio remains poorly determined as described in Sec. 3.1. Selected lightcurve fits are presented in Fig. 23.

Our sidereal period for Delvaux agrees with the partial model of Āurech et al. (2018), but our pole latitudes are more than 15 degrees farther south. Āurech et al. (2019) revisited the modeling of Delvaux and reported a sidereal period that agrees with ours but with a pair of poles having latitudes comparable to the previous partial model, 20° to 25° farther north than our solutions.

3.19. (2144) Marietta

For spin vector and shape analysis of Marietta, the lightcurves reported in this work and the data reported by Slivan et al. (2008) and Arredondo et al. (2014) were supplemented with an unpublished lightcurve recorded during the 2010 apparition (data provided by R. Roy and R. Behrend).

The available epoch data yield an unambiguous sidereal rotation period and prograde spin, with the maximum epoch interval corresponding to 28074 sidereal rotations. CI and SPA agree that the pole is at a high north ecliptic latitude, but the CI pole regions are indistinct. Fitting from trial initial poles chosen within the regions “by eye” yields a variety of statistically indistinguishable solutions without consistent convergence to indicate a favored pole location, and often having peculiar model shapes.

While exploring how to more deliberately identify an initial value for the pole location fitting, it was noticed that the χ^2 contours results from an analysis of the lightcurve data set using the simultaneous amplitude-magnitude-aspect (SAM) method of Drummond et al. (1988) resembled the outlines of the CI pole region. Ultimately an approach described by Slivan et al. (2003) which combines the SPA method with the SAM method was used to choose the initial location for the pole, from which the CI fitting converged within one degree of arc. The pole errors were estimated based on the extents of the portions of the CI solution regions that satisfy the expected symmetry.

The converged pole solution for Marietta is at a latitude high enough that the lightcurves provide only limited information to scale the model shape in the direction along the polar axis, leaving the CI shape determination sensitive to the b/c axial ratio of the initial ellipsoid. Therefore the same approach that was used to obtain model shapes for the program objects having the highest-latitude poles also was used for Marietta. Selected lightcurve fits are presented in Fig. 24.

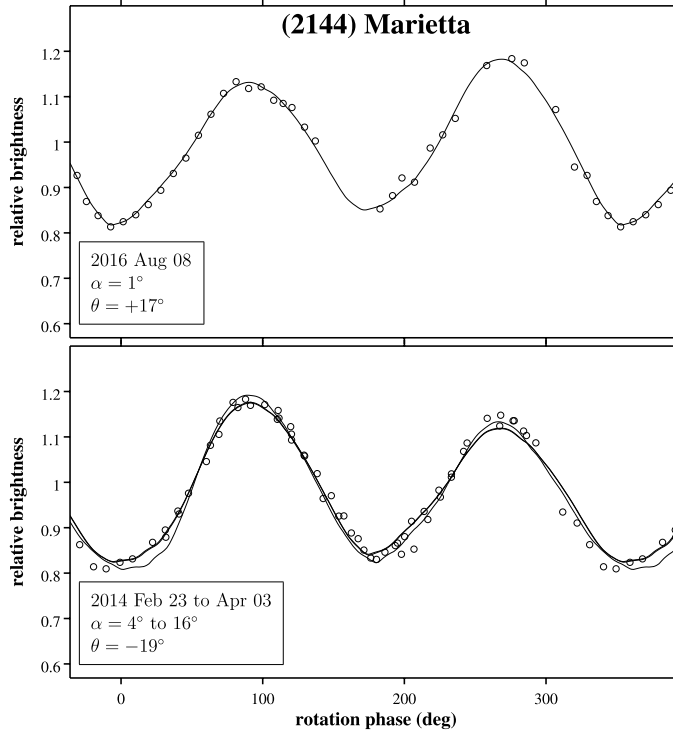


Figure 24: The same as Fig. 6 but for (2144) Marietta with a pole P_1 at $(145^\circ; +72^\circ)$. The RMS error of the fit corresponds to 0.021 mag.

Our sidereal period agrees with a model solution reported by Āurech et al. (2020), but our pole locations differ from theirs in a curious way: although the differences are both mainly in ecliptic latitude, our P_1 is south 6° ($\sim 3\times$ estimated error) while our P_2 is in the opposite direction, north 5° ($\sim 2\times$ estimated error). It is instructive to note that their pole solutions depart from symmetry with respect to the PGC pole by 10 degrees of arc, which suggests that there might be a systematic problem with at least one of them.

3.20. (2209) Tianjin

For spin vector and shape analysis of Tianjin the lightcurves reported in this work were supplemented with the lightcurves recorded in 1996 by Florczak et al. (1997). Analysis of the combined set of epochs unambiguously identifies the sidereal period and prograde rotation, for which the maximum epoch interval corresponds to 18703 sidereal rotations.

Tianjin's spin pole orientation is close enough to the north ecliptic pole that the pole longitudes are only weakly distinguished, and determining the reported b/c axial ratio of the model shape required the same approach described in Sec. 3.1 that was used for the program objects having the highest-latitude poles. Selected lightcurve fits are presented in Fig. 25.

Our sidereal period agrees with a model solution reported by Āurech et al. (2019), but our P_2 is 12° farther north in latitude and 16 degrees of arc away overall from their single reported pole location.

4. Discussion

4.1. Comparison with sparse-data period and pole determinations

As noted in the Introduction, spin vector determinations based on sparse-data analysis approaches have been reported in the literature for fifteen of the observing program objects (Hanuš et al., 2011, 2013; Āurech et al., 2016, 2018; Āurech and Hanuš, 2018; Āurech et al., 2019, 2020), providing an opportunity to compare independent solutions based on the same underlying modeling assumptions and convex inversion analysis algorithm, but using the different data sets. The sparse-data results were compared individually with their counterpart results from this work in the

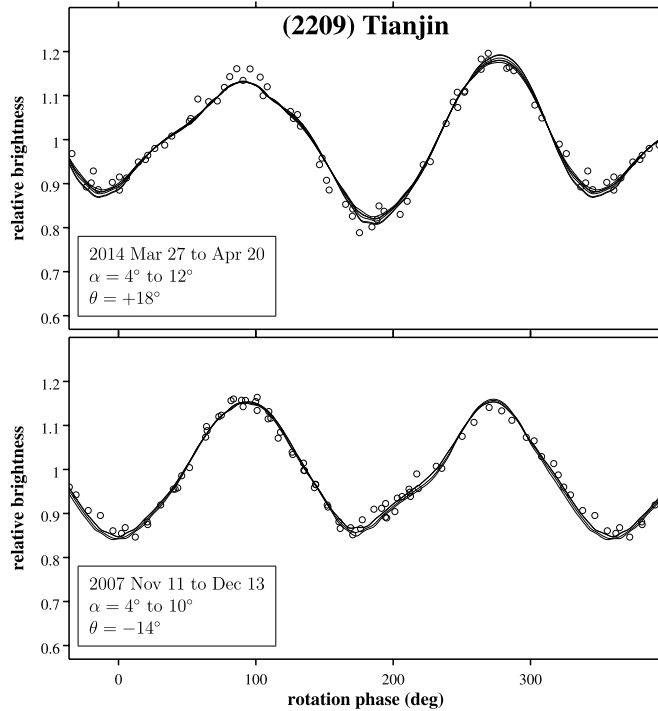


Figure 25: The same as Fig. 6 but for (2209) Tianjin with a pole P_1 at $(19^\circ; +68^\circ)$. The RMS error of the fit corresponds to 0.022 mag.

descriptions of the program objects' spin vector analyses in Secs. 3.3–3.20; here in this section the comparisons are discussed together as a population sample.

Sidereal rotation periods. Long time intervals available in the lightcurve data sets assembled for the observing program objects increase the numbers of elapsed rotations and reduce the period uncertainties—four of our program solution periods are 10 or more times more precise than the corresponding sparse-data periods, and fourteen more are between 3 and 10 times improved. The period results themselves for each object are in mainly good agreement; 17 of the 19 periods agree within their estimated errors. The two remaining pairs of period solutions each systematically differ by five to six times their errors, corresponding to an 11% fraction of false positives per the terminology of Āurech et al. (2018). Both of these sparse-data periods are close to alias periods found during the analyses reported in this work.

Spin pole locations. Histograms showing the distributions of the angular distances between the spin poles from our observing program and those based on analyses of sparse data sets are presented in Fig. 26. The small mean signed differences of the pole longitudes and latitudes of -2 and $+2$ degrees of arc, respectively, indicate that the agreement of pole coordinates is good in the average. The differences' RMS dispersions of ± 15 and ± 13 degrees of arc, respectively, are comparable to each other and to the RMS dispersion ± 17 degrees of arc of the unsigned angular distances between corresponding pole locations. The similarity of the dispersions suggests ~ 15 degrees of arc as an estimated external error for each pole coordinate, based on the comparison with the pole determinations from our observing program data sets containing mainly dense lightcurves.

Comparing the external error with estimated internal pole errors is not entirely straightforward, partly because the CI calculations do not admit analytic formal Gaussian internal errors for individual pole solutions. Instead of error estimates for each pole location, Hanuš et al. (2011) and Hanuš et al. (2013) report pole errors as ranges of the typical uncertainties that one can expect from CI for models based mainly on sparse data. The estimates in the latter paper are the more inclusive, reporting longitude uncertainties as 5–10 degrees of arc, latitude uncertainties as 5–20 degrees of arc, and pole direction uncertainties as 10–20 degrees of arc. These ranges seem to be the best available information as uncertainties also for the sparse-data poles reported in the subsequent four papers that similarly do not include individual error estimates (Āurech et al., 2016, 2018; Āurech and Hanuš, 2018; Āurech et al., 2019), for a total of thirteen of the objects among those studied in the six aforementioned papers that also are included in our observing

Spin vectors in the Koronis family: IV.

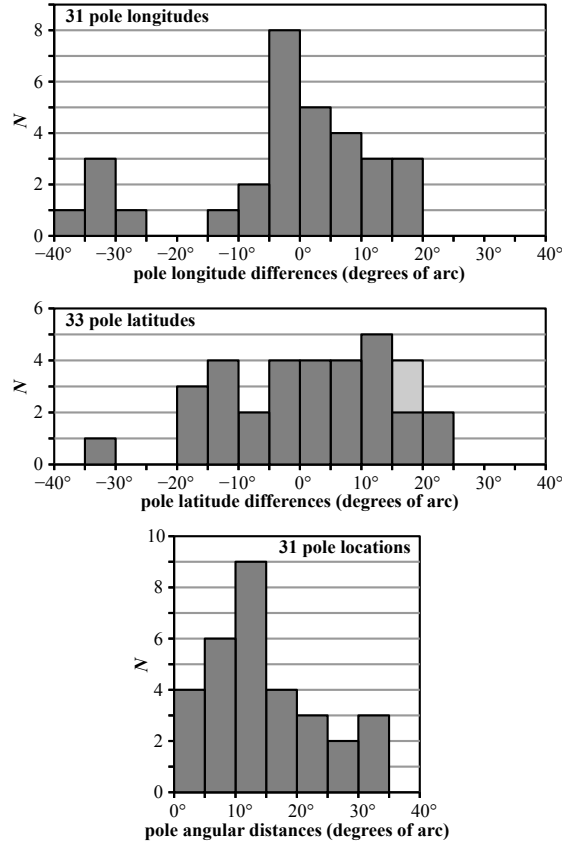


Figure 26: Distributions of angular distances between spin poles from the observing program and sparse-data results in the literature for the same objects. (upper graph) Pole longitude signed differences; the distribution mean is -2 ± 15 degrees of arc. (center graph) Pole latitude signed differences; lighter grey color represents differences from sparse-data partial solutions. The distribution mean is $+2 \pm 13^\circ$. (lower graph) Unsigned angular distances between pole locations; the root-mean-squared angular difference is 17 degrees of arc.

program. The RMS dispersion of the individual latitude differences between the program and sparse-data spin poles is within the reported range for the latitude uncertainties; however, the corresponding dispersion of ± 15 degrees of arc of the longitude differences is greater than the range 5–10 degrees of arc estimated for the longitude uncertainties, suggesting that the reported range for the longitude coordinate errors of the sparse-data spin poles is an underestimate. For the remaining two observing program objects, Āurech et al. (2020) described a Monte-Carlo approach to estimate individual errors for the pairs of pole locations that they reported. 50% (two of four) of these longitudes and 75% (three of four) of these latitudes are within twice their estimated errors from our corresponding results; each of the four poles is within 10 degrees of arc of our corresponding pole location.

4.2. Spin vector sample

The pole solutions for the observing program objects, together with the previously published results summarized in Table 11, comprise a sample of 34 spin vectors in the Koronis family. When sorted by decreasing brightness according to the catalog absolute magnitudes H in Tables 4 and 11 the sample includes the brightest 32 family members, complete to $H \approx 11.3$. The two remaining program objects also had been originally identified as part of the completeness sample, but improvements to catalog absolute magnitudes during the years-long observing program have moved the objects relatively fainter in the brightness sequence so that the sample at present includes 34 of the brightest 36 family members. The stability of the bulk of the identifications of which objects are the brightest members supports confidence in the completeness of the sample.

Table 11

Previously published spin periods and obliquities of Koronis family members based on densely-sampled lightcurves.

Asteroid	Catalog <i>H</i> ^a	Period (h)	Spin obliquity	Ref.
(158) Koronis	9.22	14.206	159°	b
(167) Urda	9.23	13.061	163°	b
(208) Lacrimosa	9.19	14.086	23°	c
(243) Ida	9.93	4.634	156°	d
(263) Dresda	10.23	16.814	16°	e
(277) Elvira	9.90	29.691	167°	e
(311) Claudia	10.00	7.532	50°	b
(321) Florentina	10.12	2.871	154°	b
(462) Eriphyla	9.38	8.659	51°	e
(534) Nassovia	9.70	9.469	42°	e
(720) Bohlinia	9.66	8.919	50°	b
(832) Karin	11.29	18.352	42°	f
(1223) Neckar	10.59	7.821	47°	b
(1289) Kutaïssi	10.65	3.624	165°	e
(1443) Ruppina	11.14	5.879	11°	g

^a Catalog absolute magnitude *H* values as described for Table 4.^b Slivan et al. (2003)^c Vokrouhlický et al. (2021)^d Binzel et al. (1993)^e Slivan et al. (2009)^f Slivan and Molnar (2012)^g Slivan (2021)

The relative brightness sequence of catalog absolute magnitudes is adopted here to represent the sequence of the objects' relative sizes, an approximation that is accurate enough for the present discussion which does not depend on the exact sequence.

It is noted that the spin vector sample includes four asteroids that were included in the observing program based on identification as family members by Mothé-Diniz et al. (2005), but are not identified in a subsequent family membership by Nesvorný (2015): (811) Nauheima, (1245) Calvinia, (1443) Ruppina, and (1848) Delvaux. Mindful that determinations of dynamical family membership involve in practice an inexact process of distinguishing true members from interlopers (Nesvorný et al., 2015), these four objects are retained in the sample as likely real members in the Koronis family based on their taxonomic classifications as S-type, which spectrally distinguish them from the C-type local background objects in the outer main belt. Nauheima, Calvinia, and Delvaux are included as S-type in the compilation by Neese (2010), and at the request of the first author of the present work a reflectance spectrum of Ruppina was obtained using the SpeX instrument (Rayner et al., 2003) for the SMASS Catalog of Asteroid Spectra,² which classifies³ as S-type in the Bus–DeMeo taxonomy (DeMeo et al., 2009).

Koronis family member (832) Karin is bright enough to be in the sample, but it is also the largest member of the Karin cluster, a second-generation asteroid family within the larger Koronis family (Carruba et al., 2016). Because of its different spin evolution history, Karin is excluded from the following discussion, leaving 33 objects in the family analysis sample.

4.3. Distributions of spin properties

A histogram of the spin vector obliquities derived for the sample is shown in Fig. 27. The small majority of retrograde spins is not statistically significant; using the binomial distribution the probability of randomly selecting at least 18 objects with the same equally-likely spin direction from of a sample of 33 objects $P(x \geq 18 \text{ or } x \leq 15)$ is

²<http://smass.mit.edu/catalog.php>³<http://smass.mit.edu/busdemeoclass.html>

Spin vectors in the Koronis family: IV.

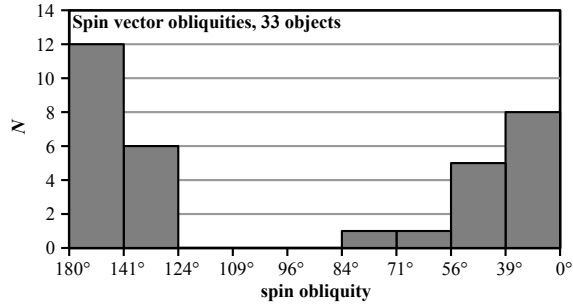


Figure 27: Distribution of spin vector north pole obliquities ϵ in the analysis sample, using bins of equal width in $\cos \epsilon$ so that poles isotropic on a sphere would give a uniform distribution.

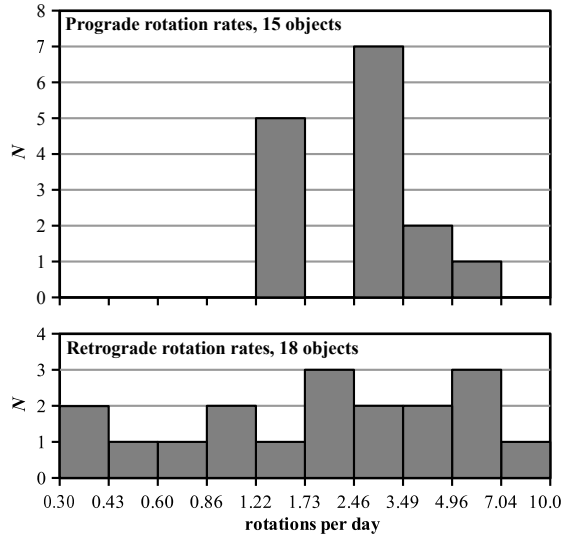


Figure 28: Distributions of rotation rates in the analysis sample for the prograde- (upper graph) and retrograde-rotating (lower graph) objects.

73%. The overall bimodal shape of the distribution favoring low spin obliquities persists from the previously-studied sample, although two higher-obliquity prograde spins introduce some asymmetry.

Histograms of the prograde and retrograde spin rates for the objects in the analysis sample are shown in Fig. 28. The spin rate distributions depend on the direction of spin because the YORP evolution histories of the prograde rotators can be subject to spin-orbit resonance trapping that does not affect the retrograde rotators (Vokrouhlický et al., 2003). The expanded sample of retrograde spins (Fig. 28, lower graph) pushes the rotation rate lower bound to $\sim 0.4 \text{ d}^{-1}$ and fills in the broad distribution of spin rates, confirming that the early impression of groupings in the retrograde rates based on the incomplete previous sample was an artifact.

In contrast, the expanded prograde rotation rate distribution (Fig. 28, upper graph) remains bimodal, and also narrower overall than the retrograde distribution. In particular, no prograde rotation rates slower than 1.4 d^{-1} are present, whereas there are six retrograde objects having slower rotations comprising one-third of the retrograde sample.

Vokrouhlický et al. (2003) found for the previous study sample that the spin rates and obliquities distributions of the largest family members are dominated by modification over 2–3 Gyr by YORP thermal radiation torques. YORP acts more quickly on smaller objects, on more elongated objects, and on objects whose shapes have more “windmill” asymmetry; thus to the extent that the objects’ shapes (Fig. 5) are comparably irregular, a more YORP-evolved distribution among the smaller objects can be expected. The spin evolution modeling results of Vokrouhlický et al. (2003) also suggested an expectation to find some prograde objects whose spin obliquity and spin rate significantly differ from the clustered spin properties previously found by Slivan (2002) for prograde Koronis members. A scatter

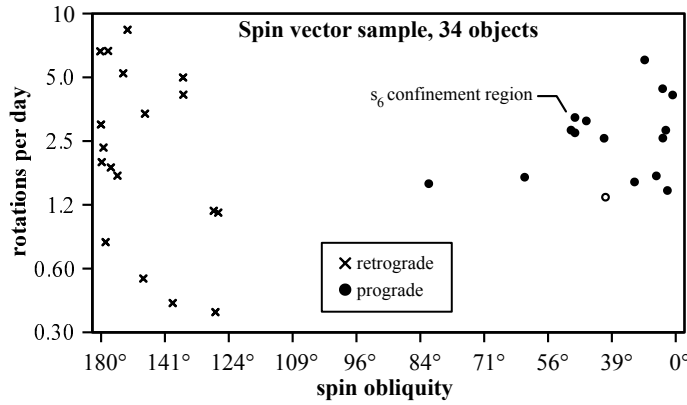


Figure 29: Spin vector sample as rotation rate vs. spin obliquity. YORP torques modify objects' locations on this graph, outward in both directions along the vertical axis by rate spin-up or spin-down, and outward in both directions along the horizontal axis by reorienting spin vectors away from the orbits' planes. The clustering of spin vectors near (45° , 3.0 d^{-1}) locates the confinement region for objects trapped in the s_6 spin-orbit resonance (Vokrouhlický et al., 2003). The open circle symbol distinguishes Karin cluster member (832) Karin which is excluded from the analysis sample.

plot of rotation rates vs. spin obliquities of the expanded sample of Koronis family spin vectors is shown in Fig. 29, on which is marked the confinement region for prograde spin vectors trapped in the s_6 spin-orbit resonance.

Among the retrograde rotators, the dominance of low spin obliquities avoiding the orbit planes suggests that the spins observed in the sample are qualitatively consistent with YORP evolution modeling results, with more-evolved spin rates at the fast- and slow-rotating ends of the distribution. The prograde distribution is more complicated because of the s_6 resonance already known, and perhaps also other possible resonances at longer periods and smaller obliquities.

The three fastest-spinning prograde rotators in the expanded sample—(811) Nauheima, (1443) Ruppina, and (2144) Marietta—are smaller than all of the trapped s_6 objects and have both shorter periods and smaller obliquities, consistent with being further spun up by YORP. Previously no prograde objects rotating faster than the trapped objects had been identified, although modeling had suggested that prograde rotators whose shapes cause them predominately to spin up would be unlikely to be captured into the s_6 resonance, and plausibly could evolve to fast prograde rotation instead (D. Vokrouhlický, personal communication).

Prograde rotators (1742) Schaifers and (2209) Tianjin have spin periods similar to the trapped s_6 objects, but are smaller in size. Their respective spin obliquities of 17° and 19° are significantly less than the 42° – 51° obliquities for the known trapped objects, and thus appear not to be trapped in s_6 themselves.

The five prograde-rotating analysis sample objects that spin more slowly than the s_6 -trapped objects all share similar spin periods of 14 h to 17 h, but have spin obliquities in a wide range from 16° to 82° . The largest of these objects is (208) Lacrimosa, having size comparable to the largest of the trapped objects but with a smaller spin obliquity of 23° . Lacrimosa had been previously misclassified as retrograde spin based on an incorrect sidereal period not recognized as being an alias. Vokrouhlický et al. (2021) determined its correct prograde spin vector solutions and discuss how its spin evolution differs from the other prograde objects of comparable size which are trapped in the s_6 resonance, concluding that it avoided capture in s_6 in its past and also is not presently trapped in a longer-period resonance.

Vokrouhlický et al. (2021) also discuss possible evolution paths including resonance capture and subsequent escape that could have been experienced by prograde-rotating objects smaller than Lacrimosa; Vokrouhlický et al. (2003) previously had found that prograde rotators that are smaller or more irregular than the s_6 objects that predominately spin down might already have evolved out of the weakly unstable s_6 resonance, and continued to spin down to other resonances with longer characteristic rotation periods. It could be instructive to explore such spin evolution possibilities in the YORP model for the two longer-period smaller prograde objects in the expanded sample that have smaller obliquities than the s_6 -trapped objects, (263) Dresda and (1029) La Plata with spin obliquities of 16° and 32° respectively.

The remaining two smaller longer-period prograde rotators (1100) Arnica and (1336) Zeelandia have higher spin obliquities of 62° and 82° respectively; their spin axes are closer to their orbit planes than are those of any other object of either spin direction in the analysis sample.

4.4. Conclusions

In this paper the lightcurve observations and analyses for spins and convex shape models of nineteen Koronis family members are reported, which increase the sample of determined spin vectors in the Koronis family to include 34 of the largest 36 family members, and complete it to $H \approx 11.3$ ($D \sim 16$ km) for the largest 32 members. The pole locations reported here agree on average with poles for the same objects in the literature that are based mainly on lightcurves sparsely-sampled in time from sky surveys, although the distribution of angular differences suggests that the uncertainties of the sparse-data pole longitudes are larger than the reported estimates.

Among the Koronis members in the completed size range, the distributions of retrograde rotation rates and pole obliquities appear to be qualitatively consistent with outcomes of modification by thermal YORP torques. The distribution of spin rates for the prograde rotators remains narrower than that for the retrograde rotators; in particular, the absence of prograde rotators having periods longer than about 20 h is real, while among the retrograde rotators are several objects having longer periods up to about 65 h. None of the prograde objects newly added to the sample appear to be trapped in an s_6 spin-orbit resonance that is characteristic of most of the largest prograde objects (Vokrouhlický et al., 2003); these smaller objects either could have been trapped previously and have already evolved out, or have experienced spin evolution tracks that did not include the resonance.

The results reduce selection biases in the set of known spin vectors for Koronis family members, and will constrain future modeling of spin properties evolution.

A. Rotating a spin pole with respect to the PGC pole

The 3×3 rotation matrix $\mathbf{R}(\theta, \hat{\mathbf{e}})$ that rotates a vector by an angle θ about an axis direction defined by the unit vector $\hat{\mathbf{e}} = (e_x, e_y, e_z)$ is given by, for example, Cox and Hart (1986, p. 227) for which positive rotation is counterclockwise in a right-hand coordinate system. Substituting for the components of $\hat{\mathbf{e}}$ in terms of latitude ϕ and longitude λ ,

$$\begin{aligned} e_x &= \cos \phi \cos \lambda \\ e_y &= \cos \phi \sin \lambda \\ e_z &= \sin \phi \end{aligned} \quad (1)$$

yields the elements of the matrix $\mathbf{R}(\theta, \phi, \lambda)$ that rotates a vector by an angle θ about an axis direction with latitude ϕ and longitude λ :

$$\mathbf{R}(\theta, \phi, \lambda) = \begin{bmatrix} R_{11} & R_{12} & R_{13} \\ R_{21} & R_{22} & R_{23} \\ R_{31} & R_{32} & R_{33} \end{bmatrix} \quad (2)$$

$$\begin{aligned} R_{11} &= 1 - (1 - \cos \theta)(1 - \cos^2 \lambda \cos^2 \phi) \\ R_{12} &= \sin \lambda \cos \lambda \cos^2 \phi(1 - \cos \theta) - \sin \phi \sin \theta \\ R_{13} &= \cos \lambda \sin \phi \cos \phi(1 - \cos \theta) + \sin \lambda \cos \phi \sin \theta \\ R_{21} &= \sin \lambda \cos \lambda \cos^2 \phi(1 - \cos \theta) + \sin \phi \sin \theta \\ R_{22} &= 1 - (1 - \cos \theta)(1 - \sin^2 \lambda \cos^2 \phi) \\ R_{23} &= \sin \lambda \sin \phi \cos \phi(1 - \cos \theta) - \cos \lambda \cos \phi \sin \theta \\ R_{31} &= \cos \lambda \sin \phi \cos \phi(1 - \cos \theta) - \sin \lambda \cos \phi \sin \theta \\ R_{32} &= \sin \lambda \sin \phi \cos \phi(1 - \cos \theta) + \cos \lambda \cos \phi \sin \theta \\ R_{33} &= 1 - \cos^2 \phi(1 - \cos \theta) \end{aligned}$$

The photometric great circle (PGC) symmetry plane of observations of an asteroid is related to its orbit elements by $\Omega_{\text{PGC}} \approx \Omega$ and $i_{\text{PGC}} \approx i(1 + (1/2a))$ (Magnusson et al., 1989). To rotate a spin pole with respect to the PGC pole, first rotate the vector direction $\hat{\mathbf{p}}$ of the pole ecliptic coordinates into the PGC coordinate system by

$$\hat{\mathbf{q}} = \begin{bmatrix} q_x \\ q_y \\ q_z \end{bmatrix} = \mathbf{R}(-i_{\text{PGC}}, 0, \Omega_{\text{PGC}})\hat{\mathbf{p}} \quad (3)$$

The rotated pole direction $\hat{\mathbf{f}}$ in ecliptic coordinates that is 180° away in PGC longitude from $\hat{\mathbf{p}}$ is then

$$\hat{\mathbf{f}} = \mathbf{R}(i_{\text{PGC}}, 0, \Omega_{\text{PGC}}) \begin{bmatrix} -q_x \\ -q_y \\ q_z \end{bmatrix} \quad (4)$$

Acknowledgments

We thank Edward Tedesco and Claes-Ingvar Lagerkvist for their invaluable help with establishing the correct time tags of their Koronis family lightcurve data from more than 45 years ago, David Vokrouhlický for helpful early discussions about YORP evolution scenarios, and Jack Drummond for calculating the moments of inertia results for the model shapes.

We thank the corps of loyal observers who recorded data at Whitin Observatory: Kathryn Neugent, Amanda Zangari, Rebekah Dawson, Kirsten Levandowski, Michaela Fendrock, Allison Youngblood, Carolyn Thayer, Kirsten Blancato, M. Claire Thoma, Anissa Benzaid, Katherine Lonergan, Molly Wasser, Kelsey Turbeville, Anne-Marie Hartt, Tim Smith, Alison Towner, Alejandra Escamilla Saldaña, Ashley Iguina, Leafia Sheraden Cox, Christine Bachman, Gillian Beltz-Mohrmann, Mariam Qazi, Rayna Rampalli, Rebecca Stoll, Sormeh Yazdi, Emily Yax, Rebecca Bernstein, Naomi Gordon, Karisa Zdanky, Helen Ressler, Chloe Shi, Cassie Miller, Floria Ngo, and Elif Samanci. At the Wallace Observatory we thank Michael Person and Timothy Brothers for allocation of telescope time and for observer instruction and support, Timothy Brothers also for making some priority observations in 2020 during the time that pandemic circumstances had closed the facility to visitors, and the Wallace summer student observers in 2021: Abigail Colclasure, Inés Escobedo, Aidan Henopp, Rory Knight, and Andi Mitchell.

Participation of coauthors M. Hosek, A. Sokol, and M. Kurzner was supported by the National Science Foundation under Grant Nos. AST-0647325 and AST-1005024. Partial support for this work was provided by the U.S. Department of Defense's Awards to Stimulate and Support Undergraduate Research Education (ASSURE) program in collaboration with the National Science Foundation's Research Experiences for Undergraduates program. Coauthor S. Maynard, observer R. Dawson, and observer K. Neugent were supported by Sophomore Early Research Program grants from the Wellesley College Office of the Dean of the College. Student service observers at Whitin Observatory were supported in part by grants from the Massachusetts Space Grant Consortium. The student observers at Wallace Observatory were supported by a grant from MIT's Undergraduate Research Opportunities Program. Use of the PROMPT telescopes for program observations was made possible by support from the Robert Martin Ayers Science Fund. The observations made by coauthor A. Russell were funded by a Theodore Dunham, Jr. Grant of the Fund for Astrophysical Research. Coauthor F. Wilkin received funding from the Faculty Research Grant at Union College.

The spectrum of (1443) Ruppina utilized for this publication was obtained and made available by the MITHNEOS MIT-Hawaii Near-Earth Object Spectroscopic Survey. The IRTF is operated by the University of Hawaii under contract 80HQTR19D0030 with the National Aeronautics and Space Administration. The MIT component of this work is supported by NASA Grant 80NSSC18K0849. The taxonomic type result for the spectrum was determined using a Bus-DeMeo Taxonomy Classification Web tool by Stephen M. Slivan, developed at MIT with the support of National Science Foundation Grant 0506716 and NASA Grant NAG5-12355.

Opinions, findings, and conclusions or recommendations expressed in this material are those of the author(s) and do not necessarily reflect the views of NASA or the National Science Foundation.

Data Availability

Datasets related to this article can be found at <http://smass.mit.edu/slivan/lcdata.html>

References

- Arredondo, A., Hartt, A.M., Yazdi, S., 2014. Rotation periods and R magnitudes of three Koronis family members. *Minor Planet Bulletin* 41, 252–254.
- Belton, M.J.S., Chapman, C.R., Klaasen, K.P., Harch, A.P., Thomas, P.C., Veverka, J., McEwen, A.S., Pappalardo, R.T., 1996. Galileo's encounter with 243 Ida: An overview of the imaging experiment. *Icarus* 120, 1–19.
- Binzel, R.P., 1987. A photoelectric survey of 130 asteroids. *Icarus* 72, 135–208.
- Binzel, R.P., 1988. Collisional evolution in the Eos and Koronis asteroid families: Observational and numerical results. *Icarus* 73, 303–313.

- Binzel, R.P., 1990. An investigation of spin vector alignment in the Koronis family, in: Lagerkvist, C.I., Richman, H., Lindblad, B.A. (Eds.), *Asteroids, Comets, Meteors III*. Uppsala Universitet, pp. 15–18.
- Binzel, R.P., Slivan, S.M., Magnusson, P., Wisniewski, W.Z., Drummond, J., Lumme, K., Barucci, M.A., Dotto, E., Angeli, C., Lazzaro, D., Mottola, S., Gonano-Beurer, M., Michałowski, T., De Angelis, G., Tholen, D.J., Martino, M.D., Hoffman, M., Geyer, E.H., Velichko, F., 1993. Asteroid 243 Ida: Ground-based photometry and a pre-Galileo physical model. *Icarus* 105, 310–325.
- Bowell, E., Hapke, B., Domingue, D., Lumme, K., Peltoniemi, J., Harris, A.W., 1989. Application of photometric models to asteroids, in: Binzel, R.P., Gehrels, T., Matthews, M.S. (Eds.), *Asteroids II*. University of Arizona Press, Tucson, Arizona. chapter III, pp. 524–556. Appendix: The IAU Two-Parameter Magnitude System for Asteroids.
- Carruba, V., Nesvorný, D., Vokrouhlický, D., 2016. Detection of the YORP effect for small asteroids in the Karin cluster. *The Astronomical Journal* 151, A164.
- Cox, A., Hart, R.B., 1986. *Plate Tectonics: How It Works*. Blackwell Scientific Publications, Palo Alto, California.
- Degewij, J., Tedesco, E.F., Zellner, B., 1979. Albedo and color constraints on asteroid surfaces. *Icarus* 40, 364–374.
- DeMeo, F.E., Binzel, R.P., Slivan, S.M., Bus, S.J., 2009. An extension of the Bus asteroid taxonomy into the near-infrared. *Icarus* 202, 160–180.
- Drummond, J.D., 2014. Precessing asteroids from radius vector models?, in: *Division for Planetary Sciences Meeting #46 Abstracts*, American Astronomical Society.
- Drummond, J.D., Weidenschilling, S.J., Chapman, C.R., Davis, D.R., 1988. Photometric geodesy of main-belt asteroids. II. Analysis of lightcurves for poles, periods, and shapes. *Icarus* 76, 19–77.
- Đurech, J., Hanuš, J., 2018. Reconstruction of asteroid spin states from Gaia DR2 photometry. *Astronomy and Astrophysics* 620, A91.
- Đurech, J., Hanuš, J., Alf-Lagoa, V., 2018. Asteroid models reconstructed from the Lowell Photometric Database and WISE data. *Astronomy and Astrophysics* 617, A57.
- Đurech, J., Hanuš, J., Oszkiewicz, D., Vančo, R., 2016. Asteroid models from the Lowell photometric database. *Astronomy and Astrophysics* 587, A48.
- Đurech, J., Hanuš, J., Vančo, R., 2019. Inversion of asteroid photometry from Gaia DR2 and the Lowell observatory photometric database. *Astronomy and Astrophysics* 631, A2.
- Đurech, J., Kaasalainen, M., Warner, B.D., Fauerbach, M., Marks, S.A., Fauvaud, S., Fauvaud, M., Vugnon, J., Pilcher, F., Bernasconi, L., Behrend, R., 2009. Asteroid models from combined sparse and dense photometric data. *Astronomy and Astrophysics* 493, 291–297.
- Đurech, J., Tonry, J., Erasmus, N., Denneau, L., Heinze, A.N., Flewelling, H., Vančo, R., 2020. Asteroid models reconstructed from ATLAS photometry. *Astronomy and Astrophysics* 643, A59.
- Florczak, M., Dotto, E., Barucci, M.A., Birlan, M., Erikson, A., Fulchignoni, M., Nathues, A., Perret, L., Thebault, P., 1997. Rotational properties of main belt asteroids: photoelectric and CCD observations of 15 objects. *Planetary and Space Science* 45, 1423–1435.
- Hanuš, J., Brož, M., Đurech, J., Warner, B.D., Brinsfield, J., Durkee, R., Higgins, D., Koff, R.A., Oey, J., Pilcher, F., Stephens, R., Strabla, L.P., Ulisse, Q., Girelli, R., 2013. An anisotropic distribution of spin vectors in asteroid families. *Astronomy and Astrophysics* 559, A134.
- Hanuš, J., Đurech, J., Brož, M., Warner, B.D., Pilcher, F., Stephens, R., Oey, J., Bernasconi, L., Casulli, S., Behrend, R., Polishook, D., Henych, T., Lehký, M., Yoshida, F., Ito, T., 2011. A study of asteroid pole-latitude distribution based on an extended set of shape models derived by the lightcurve inversion method. *Astronomy and Astrophysics* 530, A134.
- Hasselmann, P.H., Carvano, J.M., Lazzaro, D., 2012. SDSS-based asteroid taxonomy V1.1. EAR-A-I0035-5-SDSSTAX-V1.1, NASA Planetary Data System.
- Kaasalainen, M., Torppa, J., 2001. Optimization methods for asteroid lightcurve inversion. I. Shape determination. *Icarus* 153, 24–36.
- Kaasalainen, M., Torppa, J., Muinonen, K., 2001. Optimization methods for asteroid lightcurve inversion. II. The complete inverse problem. *Icarus* 153, 37–51.
- Kim, M.J., Choi, Y.J., Moon, H.K., Byun, Y.I., Brosch, N., Kaplan, M., Kaynar, S., Uysal, Ö., Güzel, E., Behrend, R., Yoon, J.N., Mottola, S., Hellmich, S., Hincse, T.C., Eker, Z., Park, J.H., 2014. Rotational properties of the Maria asteroid family. *Astronomical Journal* 147, A56.
- Kryszczyńska, A., 2013. Do Slivan states exist in the Flora family? II. Fingerprints of the Yarkovsky and YORP effects. *Astronomy and Astrophysics* 551, A102.
- Kryszczyńska, A., La Spina, A., Paolicchi, P., Harris, A.W., Breiter, S., Pravec, P., 2007. New findings on asteroid spin-vector distributions. *Icarus* 192, 223–237.
- Lagerkvist, C.I., 1978. Photographic photometry of 110 main belt asteroids. *Astronomy and Astrophysics Supplement* 31, 361–381.
- Lagerkvist, C.I., Barucci, M.A., Capria, M.T., Fulchignoni, M., Guerriero, L., Perozzi, E., Zappalà, V., 1987. Asteroid Photometric Catalogue (Original Catalogue). Consiglio Nazionale Delle Ricerche, Rome, Italy. (on-line version).
- Lagerkvist, C.I., Magnusson, P., 1990. Analysis of asteroid lightcurves. II. Phase curves in a generalized HG-system. *Astronomy and Astrophysics Supplement* 86, 119–165.
- Lagerkvist, C.I., Magnusson, P., 2011. Asteroid Photometric Catalog V1.1. NASA Planetary Data System, EAR-A-3-DDR-APC-LIGHTCURVE-V1.1.
- Landolt, A.U., 1983. *UBVRI* photometric standard stars around the celestial equator. *The Astronomical Journal* 88, 439–460.
- Landolt, A.U., 1992. *UBVRI* photometric standard stars in the magnitude range $11.5 < V < 16.0$ around the celestial equator. *The Astronomical Journal* 104, 340–371.
- Magnusson, P., Barucci, M.A., Drummond, J.D., Lumme, K., Ostro, S.J., Surdej, J., Taylor, R.C., Zappalà, V., 1989. Determination of pole orientation and shapes of asteroids, in: Binzel, R.P., Gehrels, T., Matthews, M.S. (Eds.), *Asteroids II*. University of Arizona Press, Tucson, Arizona. chapter II, pp. 67–96.
- Mailhot, E.A., Midkiff, A.H., 2014. Lightcurve analysis for (2713) Luxembourg. *Minor Planet Bulletin* 41, 157.
- Mothé-Diniz, T., Roig, F., Carvano, J.M., 2005. Mothé-Diniz asteroid dynamical families V1.0. EAR-A-VARGBDET-5-MOTHEFAM-V1.0, NASA Planetary Data System.
- Neese, C., 2010. Asteroid taxonomy V6.0. EAR-A-5-DDR-TAXONOMY-V6.0, NASA Planetary Data System.

- Nesvorný, D., 2015. Nesvorný HCM asteroid families V3.0. NASA Planetary Data System, EAR-A-VARGBDET-5-NESVORNYFAM-V3.0.
- Nesvorný, D., Brož, M., Carruba, V., 2015. Identification and dynamical properties of asteroid families, in: Michel, P., DeMeo, F.E., Bottke, W.F. (Eds.), *Asteroids IV*. University of Arizona Press, Tucson, Arizona, pp. 297–321.
- Rayner, J.T., Toomey, D.W., Onaka, P.M., Denault, A.J., Stahlberger, W.E., Vacca, W.D., Cushing, M.C., Wang, S., 2003. SpeX: A medium-resolution 0.8–5.5 micron spectrograph and imager for the NASA Infrared Telescope Facility. *Publications of the Astronomical Society of the Pacific* 115, 362.
- Shor, V.A. (Ed.), 1999. *Ephemerides of Minor Planets for 2000*. Russian Academy of Sciences, St. Petersburg, Russia.
- Slivan, S.M., 2002. Spin vector alignment of Koronis family asteroids. *Nature* 419, 49–51.
- Slivan, S.M., 2012. Epoch data in sidereal period determination. I. Initial constraint from closest epochs. *Minor Planet Bulletin* 39, 204–206.
- Slivan, S.M., 2013. Epoch data in sidereal period determination. II. Combining epochs from different apparitions. *Minor Planet Bulletin* 40, 45–48.
- Slivan, S.M., 2014. Sidereal photometric astrometry as efficient initial search for spin vector. *Minor Planet Bulletin* 41, 282–284.
- Slivan, S.M., 2021. Lightcurves, sidereal rotation period, spin pole, and convex model shape of Koronis family member (1443) Ruppina. *Minor Planet Bulletin* 48, 331–334.
- Slivan, S.M., Binzel, R.P., Boroumand, S.C., Pan, M.W., Simpson, C.M., Tanabe, J.T., Villastrigo, R.M., Yen, L.L., Ditteon, R.P., Pray, D.P., Stephens, R.D., 2008. Rotation rates in the Koronis family, complete to $H \approx 11.2$. *Icarus* 195, 226–276.
- Slivan, S.M., Binzel, R.P., Crespo da Silva, L.D., Kaasalainen, M., Lyndaker, M.M., Krčo, M., 2003. Spin vectors in the Koronis family: Comprehensive results from two independent analyses of 213 rotation lightcurves. *Icarus* 162, 285–307.
- Slivan, S.M., Binzel, R.P., Kaasalainen, M., Hock, A.N., Klesman, A.J., Eckelman, L.J., Stephens, R.D., 2009. Spin vectors in the Koronis family II. Additional clustered spins, and one stray. *Icarus* 200, 514–530.
- Slivan, S.M., Molnar, L.A., 2012. Spin vectors in the Koronis family III. (832) Karin. *Icarus* 220, 1097–1103.
- Taylor, R.C., 1979. Pole orientations of asteroids, in: Gehrels, T. (Ed.), *Asteroids*. University of Arizona Press, Tucson, Arizona. chapter IV, pp. 480–493.
- Tedesco, E.F., 1979. *A Photometric Investigation of the Colors, Shapes and Spin Rates of Hirayama Family Asteroids*. Ph.D. thesis. New Mexico State University.
- Tholen, D.J., 2009. Asteroid absolute magnitudes V12.0. EAR-A-5-DDR-ASTERMAG-V12.0, NASA Planetary Data System.
- Thomas, C.A., Rivkin, A.S., Trilling, D.E., Enga, M.T., Grier, J.A., 2011. Space weathering of small Koronis family members. *Icarus* 212, 158–166.
- Veeder, G.J., Matson, D.L., Owensby, P.D., Gradie, J.C., Bell, J.F., Tedesco, E.F., 1995. Eos, Koronis, and Maria family asteroids: Infrared (*JHK*) photometry. *Icarus* 114, 186–196.
- Vokrouhlický, D., Nesvorný, D., Bottke, W.F., 2003. The vector alignments of asteroid spins by thermal torques. *Nature* 425, 147–151.
- Vokrouhlický, D., Ďurech, J., Hanuš, J., Ferrais, M., Jehin, E., Benkhaldoun, Z., 2021. (208) Lacrimosa: A case that missed the Slivan state? *Astronomy and Astrophysics* 649, A45.